UC San Diego
UC San Diego Electronic Theses and Dissertations

Title

Informing Unmanned Underwater Vehicle Pre-Mission Planning with Environmentally Aware Simulations

Permalink

Author

Kitchen, Sean

Publication Date

2023

Peer reviewed|Thesis/dissertation

UNIVERSITY OF CALIFORNIA SAN DIEGO

Informing Unmanned Underwater Vehicle Pre-Mission Planning with Environmentally Aware
Simulations

A thesis submitted in partial satisfaction of the
requirements for the degree Master of Science

in

Oceanography

by

Sean Kitchen

Committee in charge:

        Eric Terrill, Chair
        Sophia Merrifield, Co-Chair
        Mark Anderson

2023

The thesis of Sean Kitchen is approved, and it is acceptable in quality and form for publication on microfilm and electronically.

University of California San Diego

2023

TABLE OF CONTENTS

LIST OF FIGURES

LIST OF TABLES

have had an outsized impact on me, my family, and my way of thinking, and I will forever be grateful.

Finally, I would like to express my heartfelt gratitude to my wife Lauren, and my boys Leith and Edison for their unwavering support throughout this journey. Departing from the normal flight pattern of workups and deployments, I know you thought this would be easy in comparison. A steady diet of all-nighters, late days in the labs, and weeks away doing field experiments made this more taxing than expected. You responded in the best way imaginable—with patience and encouragement. Your sacrifices have allowed me to focus on my studies and pursue my dreams. Thank you.

VITA

2011	B.S. History, United States Naval Academy
2011–2013	Surface Warfare Officer, US Navy
2013–2023	Naval Special Warfare Officer, US Navy
2021–2023	Graduate Student Researcher Scripps Institution of Oceanography, University of California San Diego
2023	M.S. Oceanography, Scripps Institution of Oceanography, University of California San Diego

PUBLICATIONS

J. Chang et al., "Power Efficiency Autonomy for Long Duration AUV Operation", in 2022 IEEE/OES Autonomous Underwater Vehicles Symposium (AUV), Sep. 2022, pp. 1–6. doi: 10.1109/AUV53081.2022.9965807.

ABSTRACT OF THE THESIS

Informing Unmanned Underwater Vehicle Pre-Mission Planning with Environmentally Aware
Simulations

by

Sean Kitchen

Master of Science in Oceanography

University of California San Diego, 2023

Eric Terrill, Chair
Sophia Merrifield, Co-Chair

Unmanned Underwater Vehicle (UUV) simulations that include environmental impacts to vehicle performance can increase mission success rates and decrease risk for the vehicle operator. In this thesis, a UUV power model and hydrodynamic model are combined in a simulation environment to create a framework for predicting vehicle performance in high currents. Field data from fixed sensors and UUV missions are used to validate the models used in the simulation tool. Results of the simulation tool are used to predict vehicle failure events, to study vehicle performance metrics, and are translated into a Tactical Decision Aid (TDA). The TDA is a powerful tool to mitigate risk in the pre-mission planning process. Two case studies in the

Mission Bay, California region are presented to demonstrate the utility of the TDA.

Chapter 1

Introduction

UUV mission planning tools frequently fail to account for the impact of ocean currents on mission duration, energy consumption, and performance characteristics. Small diameter UUVs have neither the battery capacity nor the thrust capability to overcome strong ocean currents for an appreciable duration, yet these vehicles are often required to operate in littoral regions with strong currents [3][4][5]. Coastal basins are driven by a combination of winds, remote forcing, and tides, with the latter being the most predictable. Tides are caused by the gravitational pull of the relative motion of the moon and sun around the earth.

(a) Global tidal frequency. [6]　　　　　(b) Global tidal amplitude. [6]
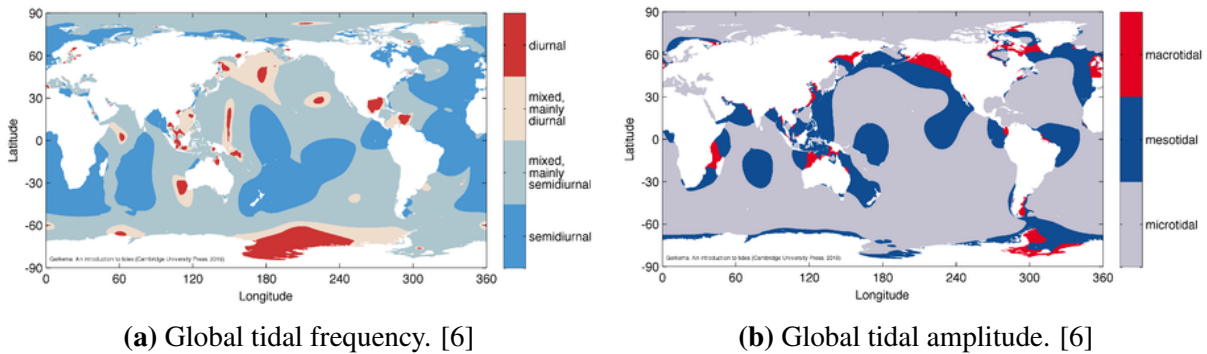
Figure 1.1. Maps of tidal (a) frequency and (b) amplitude show regions that are dominated by diurnal, semidiurnal, and mixed tides.

The frequency and amplitude of tides in Figure 1.1 impacts the volume of water entering and exiting tidal basins; that volume is referred to as a tidal prism. The volume of the tidal prism can be characterized by the equation $P = HA$ where P is inter-tidal prism volume, H is the

average tidal range, and *A* is the average surface area of the basin [7]. As *P* increases relative to the channel width, current velocity increases.

A typical UUV sortie requires three personnel, 21 man-hours, one transportation vehicle, one support vessel, and exposes the $1M vehicle to risk of damage or loss. Operating in high current environments impacts vehicle performance and poses a significant risk to vehicle safety. The only methods for mitigating these risks is operating during slack tides or programming the vehicle to run at speeds greater than the estimated maximum current for the area. These approaches fail to definitively quantify the vehicle performance or identify failures caused by environmental factors. This thesis proposes a quantitative approach to predict vehicle performance in realistic current environments, yielding opportunities for risk reduction through pre-mission planning.

1.1   Related work

The first efforts to account for environmental impacts on UUV operations used the A* algorithm to optimize the vehicle's planned path relative to bathymetry, exclusion zones, obstacles, and historical currents [8] [9]. Further research sought to optimize the vehicle path related to travel time and safety conditions using more advanced graph search approaches in three-dimensional space with strong currents [10][11] [12][13][14][15][16][17]. The U.S. Navy recognized the importance of these advances and released the "UUV Master Plan: A Vision for Navy UUV Development," which identified navigational accuracy in constrained operational areas and energy management on long duration missions as critical technology issues [18]. Vehicle performance relative to realistic ocean operating conditions motivated continued research and hardware advances [19][9][13][20][14][10]. Following the 2005 loss of Autosub2 UUV under the Fimbulisen ice shelf in Antarctica, researchers improved mission planning by considering ocean currents effect on risk [21]. The emerging qualitative risk studies used non-numerical representations to describe the frequency and the severity of a hazardous event

similar to the U.S. Navy's Operational Risk Management (ORM) matrix [22][23] (Figure 1.2).

Risk Assessment Matrix			PROBABILITY				
			Frequency of Occurrence Over Time				
			A Frequent (Continuously experienced)	B Likely (Will occur frequently)	C Occasional (Will occur several times)	D Seldom (Unlikely; can be expected to occur)	E Unlikely (Improbable; but possible to occur)
SEVERITY / Effect of Hazard	Catastrophic (Death, Loss of Asset, Mission Capability or Unit Readiness)	I	EH 1	EH 1	H 2	H 2	M 3
	Critical (Severe Injury or Damage, Significantly Degraded Mission Capability or Unit Readiness)	II	EH 1	H 2	H 2	M 3	L 4
	Moderate (Minor Injury or Damage, Degraded Mission Capability or Unit Readiness)	III	H 2	M 3	M 3	L 4	L 4
	Negligible (Minimal Injury or Damage, Little or No Impact to Mission Readiness or Unit Readiness)	IV	M 3	L 4	L 4	L 4	L 4
			Risk Assessment Levels				
			EH=Extremely High 1 H=High 2 M=Medium 3 L=Low 4				

Figure 1.2. ORM is a Navy risk management tool outlined in OPNAVINST 3500.39 that systematically identifies hazards and assesses mitigating factors, resulting in decisions that weigh risks against mission or task benefits [1].

A more precise assessment of risks, both in pre-mission planning and during mission execution, is offered by studies examining vehicle control in under-ice operations [24]. This work used mathematical models and data analysis techniques to quantify the probabilities and consequences of failure events. Other studies combined qualitative and quantitative approaches to evaluate risks, utilizing expert judgment and available data to assess the severity and likelihood of failure scenarios [23].

Chapter 2

Unmanned Underwater Vehicles (UUVs) and Mission Planning

2.1 Small-diameter UUV: REMUS100

The REMUS 100 UUV was used for all field testing for this thesis. The REMUS 100 is a two-man portable, modular, low-cost UUV designed for coastal survey work and is commonly used in academic, commercial, and military communities. The vehicle is 1.3 meters long, 0.2 meters in diameter, and has dry mass of 35 kilograms. The advertised range is 164 km on a single charge, and the vehicle typically operates at speeds from 1.0 to 1.5 m/s. Faster speeds and more complex payloads can reduce the range up to 15%. The platform is usually equipped with an Acoustic Doppler Current Profiler (ADCP) that is configured to operate as a Doppler Velocity Log (DVL). It may also be fitted with a conductivity-temperature-depth sensor (CTD), side scan sonar, optical backscatter pucks, and possibly other custom sensor payloads.

Mission parameters are set from a laptop loaded with Vehicle Interface Software (VIP). The VIP laptop is connected to the vehicle via wireless signal or cabled Ethernet connection. Core vehicle information is handled and logged on a "front-seat" computer that is installed by the manufacturer. Sensor data and advanced behavior data are logged within a Robotic Operating System (ROS) framework operating on a "back seat" processor. The back seat processor and programming framework have been developed and implemented by CORDC.
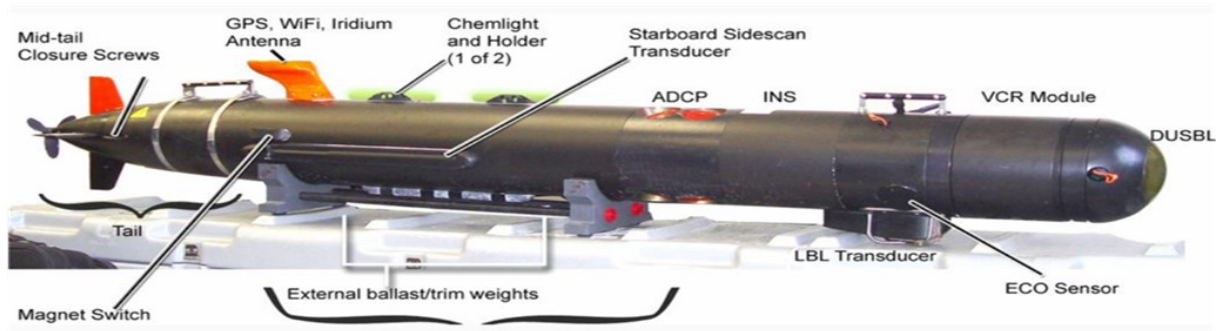
Figure 2.1. The MK18 MOD 1 unmanned underwater vehicle is a military variant of the commercially available, propeller-driven REMUS 100 UUV, and is a Program of Record principally in support of Explosive Ordnance Disposal (EOD) for teams responsible for clearing mines [2].

2.1.1 Navigation Systems

REMUS navigates using a variety of external signals, including GPS fixes when surfaced, or acoustic fixes from transponders operating in either Long Baseline (LBL) or Ultrashort Baseline (USBL) mode. Internal navigation inputs include heading information from an inertial navigation system (INS) or fluxgate compass, SOG from a DVL, a speed through water estimate using propeller speed, and a pressure sensor to provide depth. Heading accuracy is significantly improved with the INS; a Kearfott INS can increase across track navigational accuracy in dead-reckoning navigation from 2% error to 0.5% error on the REMUS 100. The INS will also report high frequency changes in vehicle pitch, roll, and yaw angles [25] [19]. DVL input (SOG) also improves navigation accuracy, but is only available when the vehicle is operated within acoustic range of the seabed. Mission parameters will determine the level of navigation accuracy required and whether transponders are needed to aid the vehicle mission.

2.2 Remus Mission Planning Tools

Mission planning is essential to the successful operation of all UUVs. To familiarize readers with UUV mission planning, this section will highlight some of the existing mission planning tools and techniques.

2.2.1 Vehicle Interface Program (VIP)
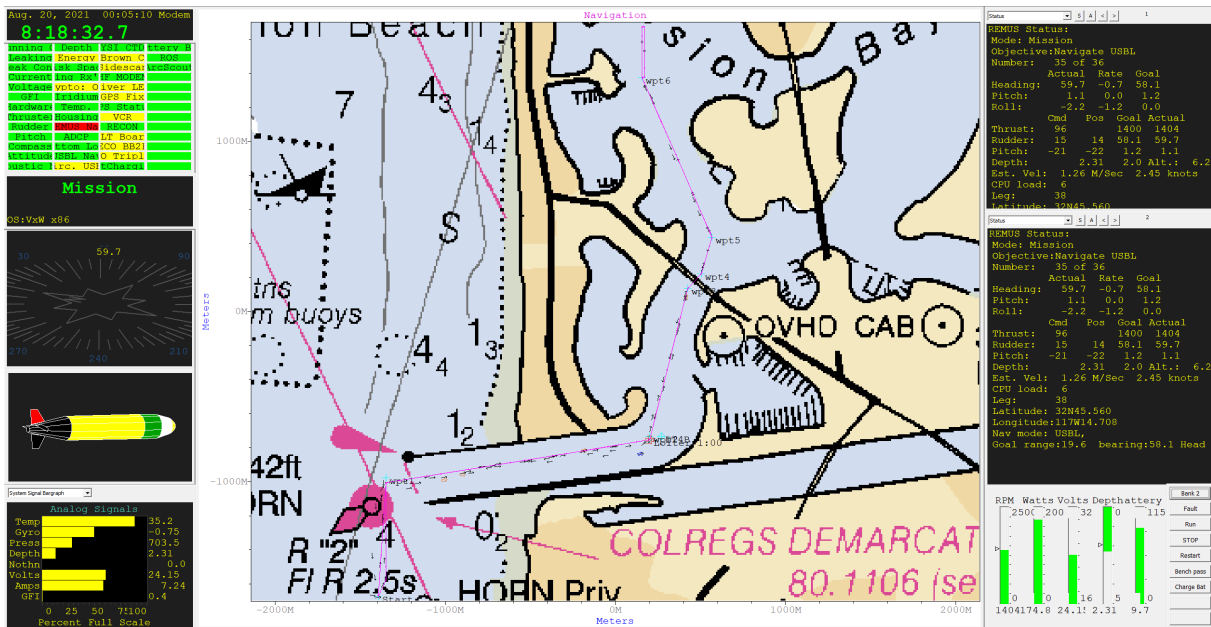
Figure 2.2. VIP graphic user interface displaying Mission Bay autonomous behavior testing.

REMUS VIP includes a graphical user interface (GUI) and is typically hosted on a ruggedized computer laptop. It is used to perform programming, mission planning, data analysis, training, documentation, vehicle maintenance, quality control checks, and troubleshooting on all REMUS vehicle types. The mission is developed and programmed in VIP, resulting in a REMUS mission file (.rmf) that must be loaded onto the vehicle backside computer before launch. An integrated text editor is provided for construction of the mission file. A map view shows the planned mission for review. The GUI displays critical system status, internal performance metrics, and the anticipated yaw/pitch/roll angles of the vehicle. Attention to detail when programming a REMUS mission is required, as small oversights can engage incorrect methods of navigation or onboard function that could have catastrophic effects on the mission. For example, if the operator does not mark 'FOLLOW TRACKLINE: YES' while making a turn into a narrow channel or harbor, the vehicle may cut the corner, resulting in collision with the breakwater or shoal.

2.2.2 Vehicle Speed Settings

REMUS vehicles have two main modes for propulsion and control. These modes allow the vehicle operator to dictate how the UUV will interact with the ocean current environment. The constant speed over ground (SOG) setting maintains a constant speed relative to the ground, and constant rotations per minute (RPM) maintains a constant speed through water. A third mode, which would vary the propeller RPM to optimize energy efficiency for distance traveled, is in development [26].

Vehicle interaction with the current environment can be best visualized with the aid of a speed triangle, depicted in Fig. 2.3. The vehicle speed relative to the ground is represented by the orange vector V_G and the angle, χ_G which defines the orientation of the vehicle's ground velocity vector relative to true north. The blue vectors u and v represent the respective east and north components of water velocity relative to the ground. The vehicle speed through water is represented by the green vector V and the angle, χ, which defines the orientation of the vehicle's velocity through water relative to north.
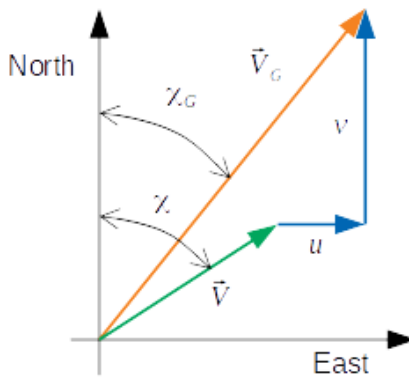
Figure 2.3. The vehicle interaction with u and v components of the water velocity is shown by the speed triangle.

Constant SOG holds V_G constant and is enabled by the DVL sensor. The DVL calculates the speed of a vehicle by measuring the Doppler shift of coded acoustic signals reflected either off water column scatterers or the sea floor. By measuring the frequency shift of the backscattered signals, the DVL can determine the velocity of the water or seabed relative to the vehicle. The

DVL derived velocity data is fed to the vehicle's navigation system to help maintain course and speed. Constant SOG is typically the preferred method of propulsion command as it allows for predictable mission times even in high current environments. When using sidescan sonar, it also provides uniform imaging resolution in the along track direction. Constant propeller speed is best utilized when attempting to run missions that require consistent energy consumption, as this mode can avoid the high propeller speeds required to compensate for head current. However, mission run times are more difficult to predict when using the constant propeller speed mode, as variable current environments may impede vehicle progress.

Chapter 3

Modeling and Simulation (M&S) Tools and Tactical Decision Aid (TDA) Development

This chapter introduces the new framework and tools that have been developed for UUV mission planning. The objective of this work is to assess whether simulations can become a reliable tool for mission planning and risk reduction in UUV operations. The framework uses in-situ data collected from the UUV and from fixed sensors to validate the simulations. This additional validation effort builds operator trust while providing quantitative metrics for mission-level evaluations.
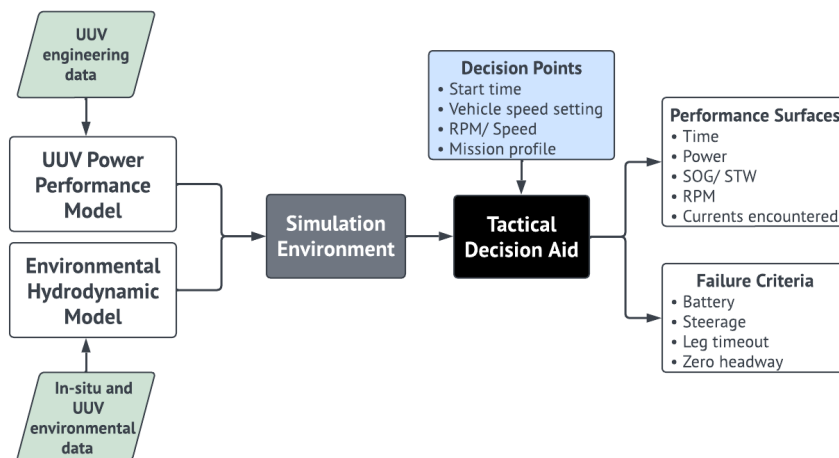
Figure 3.1. Simulation Architecture Flowchart

3.1 Simulation Architecture

Our simulation architecture includes a vehicle power model and a four-dimensional (e.g. (x,y,z,t)), high resolution hydrodynamic model representing the oceanic environment. Figure 3.1 provides a description of the primary components of the simulation. The vehicle power model was developed using accepted formulas for modeling performance of propeller-driven UUVs. Model parameters have been estimated from published literature and recent flight tests [26].

The vehicle power and environmental models are combined to form the simulation environment. The simulation can be configured to execute a single mission or an ensemble of missions with variable parameter settings. The input variables available for ensemble simulations include: mission start time, vehicle speed setting, vehicle speed, and mission profile. The output variables reported from each individual simulation are listed in the Appendix (Figure 3.2).

The performance surfaces of the single or ensemble mission simulations are logged and become available for subsequent analysis. The TDA indexes the simulation output to report bulk statistics, display performance metrics, and mark failure events in an easily readable format to inform the operator of risk and vehicle performance for a given period.

3.1.1 UUV Power Model

The instantaneous power (P) consumed by the UUV combines the power needed to move the vehicle forward and the "hotel power" (P_H) required to power on-board systems. Equation (3.1) below provides the formula that is typically used to model power for a propeller-driven UUV. The power coefficient (c_P) represents the performance of the propeller and motor controller combination. The hotel power will be assumed constant but, in practice, may vary if sensors and other electronic systems are switched on or off during the mission. Equation (3.1) also shows that power depends on the propeller speed (n), propeller diameter (d), and water density (ρ).

$$P = c_P \rho n^3 d^5 + P_H \tag{3.1}$$

The propeller advance ratio (J) defines a relationship between rate of rotation and the UUV's speed through water (V_w). This relationship is shown in Eq. (3.2). The advance ratio depends on the vehicle's drag characteristics and is constant in steady, level-depth flight. Equation (3.3) defines the vehicle SOG (V_g) as the sum of the vehicle speed through water and the water current in the direction of travel. Note that this equation assumes W_c is positive when the water current flows in the travel direction (tail or following current). Conversely, W_c will be negative when the water current opposes vehicle motion (head current).

$$J = \frac{V_w}{nd} \tag{3.2}$$

$$V_g = V_w + W_c \tag{3.3}$$

As previously introduced, the UUV configurations under study have two modes of operation. One mode sets the propeller speed to a specified constant value. The second mode holds the vehicle ground speed to a specified constant. The constant ground speed mode adjusts propeller speed to minimize the difference between the commanded value and the actual ground speed, as measured by the DVL sensor.

The instantaneous power draw will remain constant when the vehicle is operating in constant propeller speed mode. However, the vehicle ground speed may vary if the vehicle encounters any significant water current. This relationship is seen in Eq. (3.4), which combines Eqs. (3.2) and (3.3), as the speed through water will be constant with constant propeller speed.

$$V_g = Jnd + W_g \tag{3.4}$$

If the water current is constant along the mission leg, the total time to complete the leg (t_L) is found using Eq. (3.5), where d_L is the leg distance (i.e. distance between two waypoints). The total energy required to complete the leg (E_L) is given in Eq. (3.6).

$$t_L = \frac{d_L}{Jnd + W_g} \tag{3.5}$$

$$E_L = Pt_L \tag{3.6}$$

The preceding expressions demonstrate that, while the instantaneous power is constant during the constant propeller speed mode of operation, the total energy needed to complete a mission leg will largely depend on how long it takes to travel the leg distance. Equation (3.5) above shows that a tail or following current ($W_c > 0$) will reduce leg time, resulting in less energy consumed. A head current ($W_c < 0$), which opposes vehicle motion, will increase the leg time and therefore energy consumed.

The leg time will not depend on water current when the vehicle is operating in constant ground speed mode. Equation (3.7) computes the leg time for constant ground speed flight. The leg time will be reduced if the vehicle operator specifies a higher ground speed.

$$t_L = \frac{d_L}{V_g} \tag{3.7}$$

The energy required to complete a mission leg in constant ground speed mode is again established by Eq. (3.6). The leg time does not vary with water current, but the instantaneous power does vary with water current in the constant ground speed mode of operation. The instantaneous power depends on propeller speed, as shown in Eq. (3.1). The propeller speed required to maintain a given ground speed is shown as Eq. (3.8).

$$n = \frac{V_g - W_c}{Jd} \tag{3.8}$$

Equation (3.8) reveals that when water current flows in the direction of travel, ($W_c > 0$) the required propeller speed is reduced which, in turn, reduces the instantaneous power and total energy. Conversely, the required propeller speed will increase when the vehicle experiences a

12

Table 3.1. Navigation Mode Effect on Vehicle Performance

Propulsion control	Constant Ground Speed	Constant Propeller Speed
Time	constant	variable
Distance	constant	constant
Energy consumed	variable	variable
Propeller speed	variable	constant
Speed over ground	constant	variable
Speed through water	variable	constant

water current that opposes vehicle motion ($W_c < 0$). The opposing water current will therefore increase instantaneous power and the total energy required to complete the mission leg.

Table 3.1 summarizes how the two vehicle navigation modes affect vehicle performance. Navigating with a constant ground speed results in variable propeller speed, speed through water, and energy consumption. These variations result when the vehicle encounters a significant water current and the propeller speed changes to maintain the desired ground speed. In constant propeller mode, the mission time, SOG, and energy consumed become variable. Consequently, energy use will vary regardless of the navigation mode, and energy use cannot be accurately estimated unless the water current and environment are accurately represented.

3.1.2   Hydrodynamic Model - DELFT 3D

Oceanographic models can be used to simulate hydrodynamic processes in coastal and estuarine environments by representing a variety of physical processes including waves, currents, sediment transport, and freshwater transport. Advanced models can be run with complex bathymetry, including shallow water areas, channels, and tidal flats, and can include the impact of wave-driven circulation on current patterns.

The DELFT 3D hydrodynamic model is used for this study. One of the key strengths of the DELFT model is its flexibility, which allows it to be tailored to specific applications and environments. The model can be run at various resolutions— from large-scale regional simulations to small-scale local studies, and can be adapted to include different physical and environmental

parameters as needed. The model also has the ability to incorporate real-time data, such as current measurements from sensors, to improve the accuracy of simulations and predictions [27]. DELFT model output was provided by the Naval Special Warfare Mission Support Center (MSC, Imperial Beach, CA) and the Fleet Numerical Meteorology and Oceanography Center (FNMOC - Stennis Space Center, MS).

Boundary conditions for the DELFT model come from a global-scale operational ocean prediction system known as Navy Global Hybrid Coordinate Ocean Model (HYCOM). This system generates daily ocean forecasts and is an evolution of the Global Navy Coastal Ocean Model (NCOM). The system is also used by the National Oceanic and Atmospheric Administration under the name Global Real-Time Ocean Forecast System (Global RTOFS). The Global RTOFS employs a different atmospheric forcing model, or Weather Research Forecast (WRF), versus the Navy's Coupled Ocean Atmosphere Model Prediction System (COAMPS). Navy Global HYCOM is updated once per day and provides a forecast range of seven days. The system incorporates data assimilation using the Navy Coupled Ocean Data Assimilation (NCODA) system developed by NRL. The output data includes temperature, salinity, eastward and northward currents, and sea surface height. The horizontal resolution of the model is $1/12°$, while the vertical resolution consists of 40 standard depth levels. The output data are available in NetCDF file format and are produced daily at 0000Z.

3.1.3   Simulation Environment

The utility of a complete simulation environment is the ability to run large numbers of representative missions in minutes, with no residual risk. It also allows the operator to rapidly design, test, and refine mission plans or parameters [28]. The modular structure of the simulation environment allows single variables to be manipulated within a given range in a process commonly referred to as sensitivity analysis or parameter sweeping. This process systematically iterates through single or multiple variables and generates output needed to characterize mission performance. This study will conduct thousands of simulations, modifying

time and speed within a defined range, to assess the resulting changes in mission completion time, energy consumption, coverage area, or failure criteria. Statistical metrics are then used to assess vehicle performance [29].

The four standard inputs required to run the simulation environment [30] are vehicle type, environmental information, vehicle route, and vehicle speed mode setting. The simulation then uses numerical integration techniques to update the vehicle's state until the next route waypoint is reached. Following the completion of the simulation, all performance data are recorded in a twenty-five field data structure. A detailed listing of the output data fields is presented in Figure 3.2.

fieldname	description
lon	longitude [deg]
lat	latitude [deg]
depth	depth [m]
dnum	time [matlab datenum]
cog	course over ground (true heading) [deg]
phi	commanded heading [deg]
n	commanded propeller speed [rpm]
dz	change in depth [m]
dx	change in distance [m]
dt	change in time [s]
pwr	instantaneous power consumption [W]
stw	speed through water [m/s]
sog	speed over ground [m/s]
dedr	energy consumption rate [Wh/km]
Wu	eastern current [m/s]
Wv	northern current [m/s]
Wf	forward current [m/s] (with vehicle)
Ws	starboard current [m/s] (across vehicle)
leg_num	index of targeted waypoint
cum_distance	cumulative distance [m] (from start)
nrg	energy used from control [Wh]
cum_nrg_consumed	cumulative enrgy consumed [Wh] (from start)
total_dist	total covered in simulation [m]
total_nrg_consumed	total energy consumed over simulation [Wh]
start_time	start time of simulation [datenum]

Figure 3.2. Simulation output parameters

The simulation environment includes options for numerically integrating the vehicle equations of motion with respect to either time or distance increments. This study utilizes distance increments, as this option is useful when the vehicle is not expected to deviate from a rhumb line path between waypoints. In this case, the leg length or distance between waypoints does not vary within the simulation.

The geodetic position of the vehicle is then found by numerically integrating Eqs. (3.9) and (3.10) for a fixed path distance increment dR. These equations assume a spherical Earth with radius (R_E), which should be sufficient for mission legs of moderate length. The latitude (ϕ) and longitude (λ) angles determine the geodetic position of the UUV. Elapsed time is found by integrating Eq. (3.11) and the cumulative energy use is found by integrating Eq. (3.12).

$$\frac{d\phi}{dR} = \frac{1}{R_E}\cos\chi \tag{3.9}$$

$$\frac{d\lambda}{dR} = \frac{1}{R_E}\frac{\sin\chi}{\cos\phi} \tag{3.10}$$

$$\frac{dt}{dR} = \frac{1}{V_g} \tag{3.11}$$

$$\frac{dE}{dR} = \frac{P}{V_g} \tag{3.12}$$

The simulation time and geodetic location of the vehicle are used to find the water current in the direction of travel. The local water components are shown in Eq. (3.13) below as functions of latitude, longitude, and time. A linear interpolation method is used to find the water current components from the tabular data representing the DELFT model output. Note that the simulation time variable may require conversion to local time or UTC time to be consistent with the DELFT model.

$$W_c = v(\phi,\lambda,t)\cos\chi + u(\phi,\lambda,t)\sin\chi \tag{3.13}$$

3.2   Tactical Decision Aid Metrics

A valuable TDA should help the operator balance risk and reward. This work will focus on evaluating risk: in particular, the risk that the mission will not succeed as designed. The

software framework previously introduced will be used to simulate a complete UUV mission under given environmental conditions. Metrics can be constructed from the simulation results to indicate mission success or failure. By evaluating several possible operating conditions, the end user can then draw important conclusions regarding the overall risk associated with the mission before execution.

The main performance measures analyzed in this paper are: mission run time, power consumption, SOG, speed through water, RPM, relative head current, and relative tail current. Power consumption is the only universal performance surface common to all propulsion settings. Important metrics such as instantaneous power (P), cumulative energy consumed (E), and energy consumed per distance traveled (dE/dR) allow us to assess the energy efficiency of the UUV and make informed decisions regarding power management and mission duration in pre-mission planning.

3.2.1 Failure Criteria

The simulation results will be evaluated against four different criteria that are meant to identify operating conditions that have a high risk of failure. The failure criteria investigated in this study will be formulated specifically for small-diameter UUVs, like the REMUS 100. However, the failure criteria developed are general enough to be adapted to larger UUVs as well. Model parameters for the example vehicle are listed in Table 3.2.

Table 3.2. Study Vehicle Model Parameters

Parameter Name	Symbol	Value
Advance Ratio	J	0.53 [1/rev]
Propeller Diameter	d	0.14 [m]
Power Coefficient	c_P	0.13 [1/rev^3]
Water Density	ρ	1025 [kg/m^3]
Hotel Load	P_H	60 [W]

The first failure metric evaluates energy use. In particular, a potential mission failure is noted if the energy required to complete the planned mission exceeds the on-board battery

17

capacity of the UUV. As previously described, the simulation environment predicts cumulative energy by integrating Eq. (3.12) along the planned trajectory. This failure metric tests the logical expression in Eq. (3.14), where E represents cumulative energy consumption and C_B denotes the UUV's battery capacity or allocation. An operating condition is identified as failed if Eq. (3.14) is satisfied at any time during the simulation.

$$E > C_B \tag{3.14}$$

The second failure metric evaluates forward progress by testing whether the actual time required to complete a given mission leg greatly exceeds the expected time. This failure criteria safeguards the vehicle from getting stuck fighting a current that it cannot overcome. The expected leg time is computed using an assumed vehicle speed in a no current environment and the distance of the leg. Equation (3.15) compares the actual leg time t_L against the expected time to complete a leg of length d_L when the vehicle is operating in constant propeller speed mode.

The expected leg time is multiplied by a tolerance factor $k > 1$. This factor is introduced to allow the actual leg time to exceed the estimated time within an acceptable margin. A tolerance factor of $k = 2.5$ is used in this study, and is typical of the margins used in UUV guidance systems.

$$t_L > k\frac{d_L}{V_g} \quad \text{(constant propeller speed)} \tag{3.15}$$

Loss of steerage is a significant risk factor in UUV operation and can occur at low forward speeds. The vehicle is positively buoyant, and uses the horizontal stabilizer fins to counter the buoyant force. Loss of flow will cause loss of steerage control and buoyant force counterbalance. This failure metric is tested using Eq. (3.16). The assumed low speed threshold of $V_{wt} = 0.5$ m/s is based on previous experience with small-diameter vehicles. This speed threshold is equivalent to a propeller speed of 400 rev/min for the subject vehicle.

$$V_w < V_{wt} \tag{3.16}$$

The last TDA metric involves conditions that require the UUV to operate with a significant water current opposing vehicle motion. This metric is also intended to evaluate forward progress. The leg time for a vehicle operating in constant RPM propeller speed mode is given as Eq. (3.17) below. It is clear that the leg time will diverge if the denominator of this expression approaches zero. Consequently, a fourth failure metric, shown as Eq. (3.18), checks if the amplitude of the water current exceeds the vehicle's speed through water. This metric applies only when the vehicle is operating in constant propeller speed mode.

$$t_L = \frac{d_L}{V_w + W_c} \tag{3.17}$$

$$|W_c| > V_w \ \text{(constant propeller speed)} \tag{3.18}$$

In constant ground speed mode, the vehicle's propeller speed is continuously adjusted to maintain the commanded ground speed. Therefore, when faced with an opposing water current, it is possible that the required propeller speed exceeds a maximum propeller speed (n_{max}) set by the manufacturer. The resulting failure metric is presented as Eq. (3.19). It will be assumed that the maximum propeller speed for the subject UUV is 1600 rev/min. As a result, the logic test in Eq. (3.19) can be expressed as Eq. (3.20), or, equivalently, a condition involving the vehicle speed through water. This metric applies when the vehicle is in constant ground speed mode. The operating condition under test will result in a high likelihood of failure if Eq. (3.20) is satisfied at any point in the simulation.

$$n = \frac{V_w}{Jd} > n_{max} \tag{3.19}$$

$$V_w > Jdn_{max} \ \text{ or } \ V_w > 2.0 \ \text{m/s} \quad \text{(constant ground speed)} \quad (3.20)$$

Table 3.3 lists the four failure criteria that will be used to isolate operating conditions that are likely to result in a failed mission. In this table, the abbreviation cSTW represents constant speed through water V_w, or equivalently constant RPM propeller speed n. The abbreviation cSOG stands for constant ground speed V_g. Each failure condition is checked against the ensemble of simulations collected when each operating condition is varied. It will be assumed that a mission succeeds if none of the four failure metrics are triggered.

Table 3.3. Failure Criteria

Failure Type	Constant SOG	Constant STW	Criteria	Conditions
Energy	x	x	$E > C_B$	
Leg Timeout (cSTW)		x	$t_L > 2.5 \ d_L/V_g$	
Head Current (cSTW)		x	$\lvert W_c \rvert > V_w$	$W_c < 0$
Head Current (cSOG)	x		$V_w > \ 2.0 \ \text{m/s}$	
Steerage	x		$V_w < 0.5 \ \text{m/s}$	$W_c > 0$

Chapter 4

Field Tests & Simulation Results

The results of a campaign to validate the DELFT 3D Hydrodynamic Model and measure vehicle performance against the simulation are presented in this chapter. The results are extended to example missions which are used to explore criteria that may be incorporated into a TDA. In 2021 and 2022, a series of experiments were conducted in Mission Bay, California to test the vehicle power model and assess the simulation tool in a region where currents vary significantly in space and time. A fixed ADCP (Teledyne, Poway CA) was deployed to record temporal changes in the currents, and a REMUS 100 (Huntington Ingalls, Pocassett MA) was programmed to transit through the study site during different phases of the tide. The vehicle logged power consumption and navigation data for validation of the vehicle power model and modeled ocean currents. These in-situ collection data are used to assess and validate the accuracy of the DELFT 3D model. Next, the simulation is run with matching mission parameters and compared to vehicle performance metrics to quantify the accuracy of the simulation. By comparing the outcomes and metrics of the real-world missions with their simulated counterparts, insights can be gained into the effectiveness and limitations of using simulations for UUV mission planning and assessment.

4.1   Mission Bay, California

Mission Bay is a semi-enclosed body of water located in San Diego, California, with a surface area of 9.4 square kilometers and a mean water depth of 2.4 m (see Figure 4.1). A

'non-scouring' entrance channel was built in 1946 on the west side of the bay with a wide cross-sectional area to reduce the tidal currents. The average currents are less than 0.6 m/s, but can exceed 1.1 m/s [31]. The mean and diurnal tidal range is 1.1 m, with sea level variation from 0.75 m below to 2.1 m above mean lower low water [32]. The arid climate of San Diego averages 25 cm of rainfall annually, making net current outflow from fresh water input events extremely rare. The mean wave height at the mouth of the bay is generally less than 1 m, with periods between 6 and 18 seconds. However, large waves (greater than 5 m), caused by storm events coming from the west, can break inside the channel.
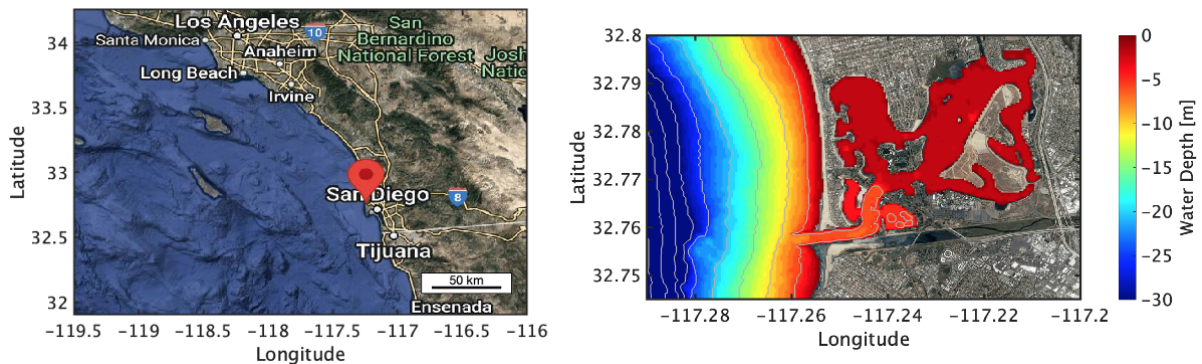
Figure 4.1. Mission Bay is located in Southern California and has bathymetric variation of less than 2 m. The coastal shelf gradually slopes to the west, reaching depths greater than 30 m only 2.5 km outside the mouth of the bay.

As a result of the complex geometry of Mission Bay, currents vary significantly in space. Figure 4.2 shows a map of the maximum currents extracted from a multi-month DELFT 3D model simulation of the tidal currents output every 10 minutes. The "hot spots" show locations where the vehicle may encounter strong currents. To study temporal variations in ocean currents, an upward-looking 1200 kHz ADCP was bottom mounted in the Mission Bay main channel from 15-Jul-2021 15:00:00 to 03-Aug-2021 21:50:00 at a nominal depth of 7 m. The measured current profiles had 35 cm vertical resolution and were ensemble averaged every 10 minutes.
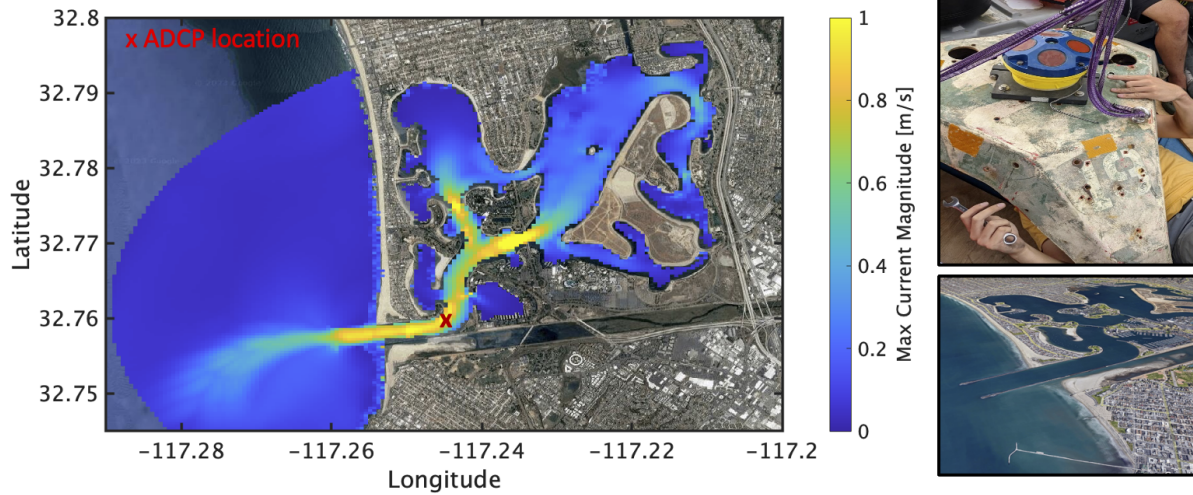
Figure 4.2. Left) Maximum water current speed simulated by DELFT 3D over a 2-month period. The channel at the mouth constricts the water flow, resulting in currents greater than 1 m/s. Top right) 1200kHz ADCP deployed at the X shown on the map. Bottom right) Aerial view of bay geometry.

Depth-averaged currents and bottom temperatures measured at the ADCP head vary both semidiurnally and diurnally (Figure 4.3). Maximum current magnitudes peak at 65cm/s during spring tide. The dominant current directions are $47°$ and $241°$. The non-reciprocal nature of these two values matches the geometry of the channel, as the ADCP was placed at the end of the inlet, where the channel makes a $115°$ turn to the north.
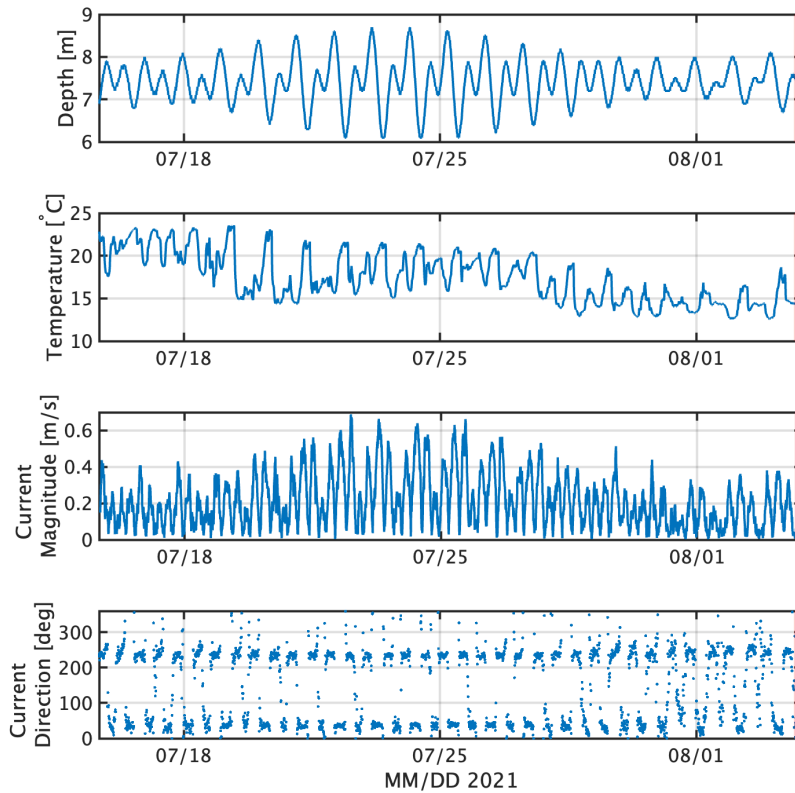
Figure 4.3. Time series of ADCP-measured sea surface height, temperature, current magnitude, and current direction (to) in Mission Bay channel are displayed. The time frame of the vehicle mission is highlighted in red. The location of the ADCP is indicated in the previous figure.

A variance ellipse computed using the depth averaged north and east velocities has a major axis direction of $43.21°$ and magnitude of 0.49 m/s (Figure 4.4). This direction is consistent with the along channel geometry, with the minor axis being cross channel. An Empirical Orthogonal Function (EOF) analysis of the vertical structure of the currents confirms that approximately 98% of the variance of the signal can be explained by mode 0 (Figure 4.4). Due to weak current variability as a function of depth, we choose to use depth-averaged currents to represent the conditions in Mission Bay.
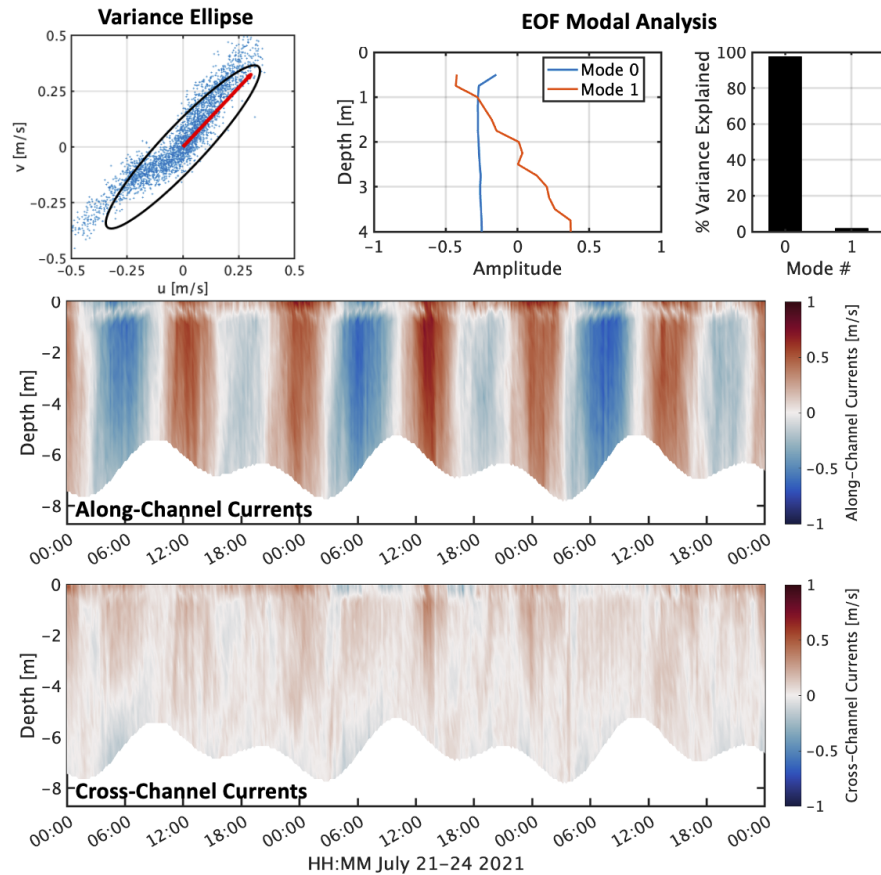
Figure 4.4. Variance ellipse fit to the depth-averaged measured velocity components shows a major axis in the along-channel direction. EOF analysis of the vertical current profiles and the vertical structure timeseries of along- and cross-channel show the strong mode 0 signal.

4.1.1 Hydrodynamic Model Validation and Verification (V&V)

To validate the DELFT 3D model output, currents measured by the ADCP are compared to those at the collocated location in the model. At the stationary ADCP location, model currents are in strong agreement with observations (Figure 4.5). To test the phase relationship, a lag-correlation is computed between the model and observed along-channel currents. (Figure 4.6). The correlation is maximum at zero lag.
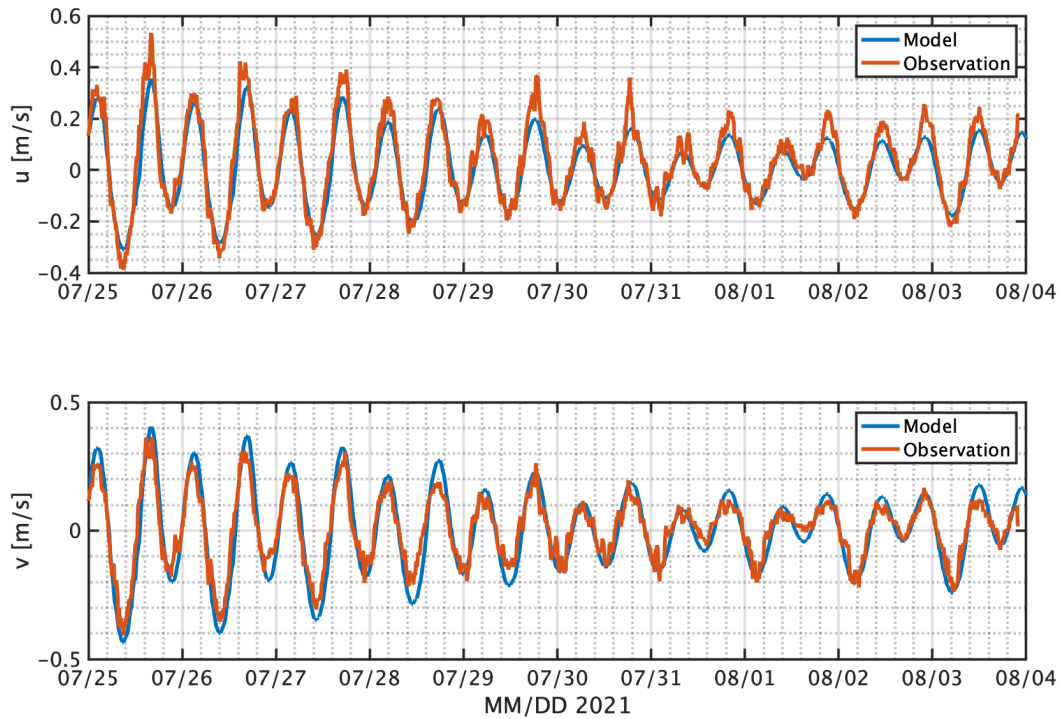
Figure 4.5. DELFT 3D model comparison to in-situ measurements shows the model accurately represents the current dynamics in the Mission Bay main channel. The comparison yields a -0.02 bias, a 0.05 RMSE, and a high cross correlation value of 0.97
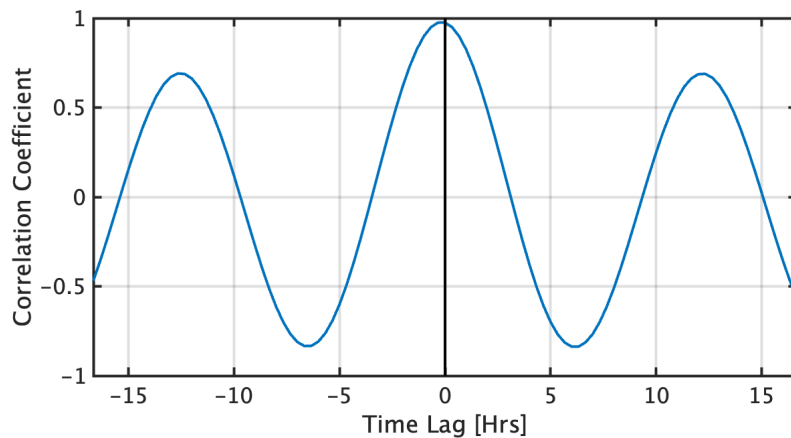
Figure 4.6. Computed phase lag between the observed and modeled currents is within the temporal resolution of the observations (10 minutes), illustrating the accuracy of DELFT 3D to predict tide changes. The phase lag is periodic at + 6 and -6 hours as a result of the periodic nature of tides.

Frequency spectral analysis of the two records is presented in Figure 4.7. The data are time-averaged to match the model resolution of twenty minutes, and the Fourier analysis is conducted over the six-week window of the ADCP deployment. Both the data and model show the four primary diurnal and semi-diurnal tidal constituents: O1, K1, M2, S2. At higher frequencies, the observations have more energy than the model, indicative of a combination of measurement noise and broadband current signals. Weak harmonics appear to be present at 3 cpd and 4 cpd (8 and 6 hour respectively). The model and data along-channel current have a correlation coefficient of 0.97.
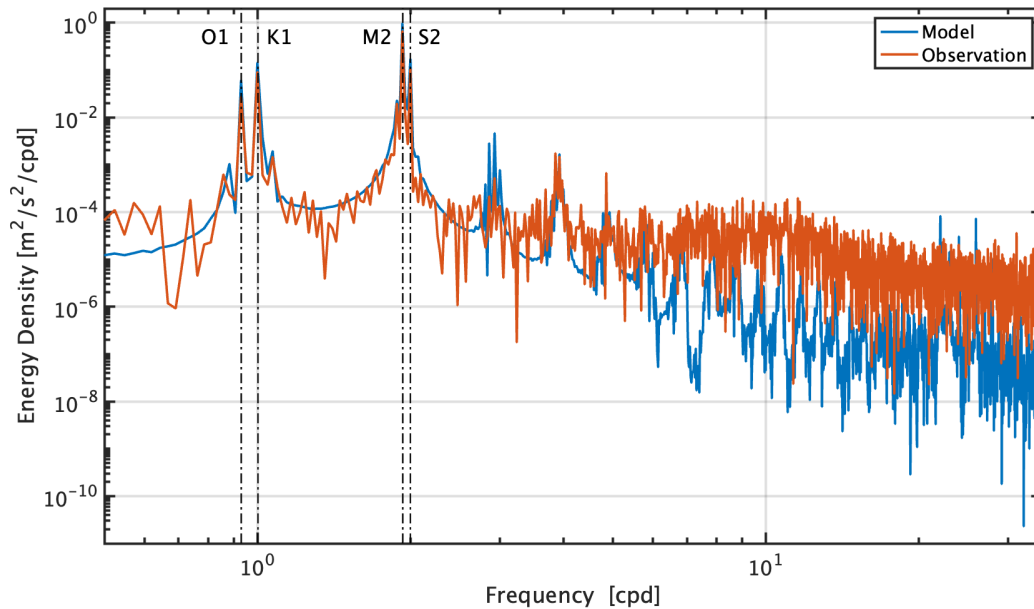
Figure 4.7. Power spectra of the along-channel, depth-averaged currents from the ADCP (red) and DELFT 3D model (blue). Both signals agree in the diurnal and semi-diurnal frequencies, however the observations have a higher noise/white spectrum at the super-tidal frequencies.

4.1.2   UUV Power Model Validation

Spatial variations of the hydrodynamic model and power consumption can be examined using engineering data from UUV sorties within Mission Bay. Sorties were programmed to conduct repeat transits in and out of the Bay using tracks similar to those shown in Figure 4.8. The vehicle missions were conducted using either constant SOG or fixed RPM propeller speed

modes of propulsion control. During these missions, the UUV was configured to record all engineering data to allow for post-mission analysis. The round-trip distance was approximately 16 km.

Figure 4.8. Track of REMUS 100 mission (orange) run on August 20, 2021 in Mission Bay, CA.

An assessment of the spatial currents is conducted using the observed head/tail current that the vehicle is exposed to during the transits. In constant propeller mode, the vehicle computer uses DVL measured bottom-track velocity compared to zero current transit speed to compute head or tail current velocity. To compare the model output against the vehicle measured apparent currents, the modeled currents at each unique time/space location are extracted and rotated into the vehicle's heading.

Figure 4.9 shows an example output of UUV testing conducted on August 20, 2021 while the vehicle was operated with a fixed propeller speed of 1400 rev/min. The observed currents range approximately $\pm$ 1 m/s while the vehicle transited through the channel. In general, the trends between the model and data are consistent; however, there are some local deviations where the model over-predicts the currents. For example, Figure 4.9 shows that there are up to 0.5

m/s differences at elapsed times of 0.8 and 1.1 hours into the mission, which corresponds to the transit into and out of Sail Bay. A small navigation error may contribute to the mismatch, but the location of the vehicle at these times is similar, and indicates a region of Mission Bay that is not well predicted by the hydrodynamic model. Further work to characterize model uncertainty in space and time is beyond the scope of this thesis.
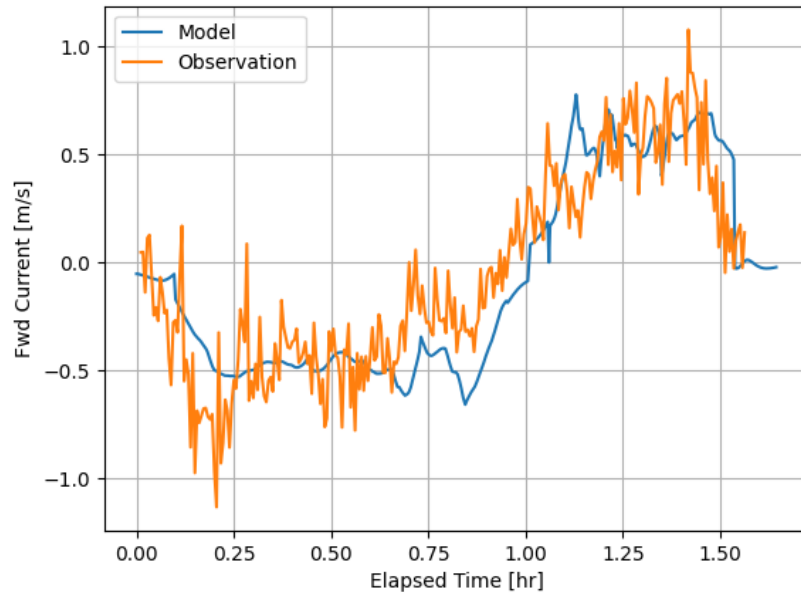
Figure 4.9. Time series of vehicle observed currents (red) and the DELFT simulated currents interpolated at the unique time/space locations of the vehicle (blue).

Figure 4.10 shows the simulated vehicle power compared to the actual power recorded on the vehicle. The simulated vehicle power is shown to be constant with time, which is expected with a constant propeller speed navigation mode. The observed power is also shown to be relatively constant throughout the mission. Nevertheless, these results demonstrate that the vehicle power model, integrated with the DELFT current model, provide a reasonable approximation of the actual vehicle characteristics.
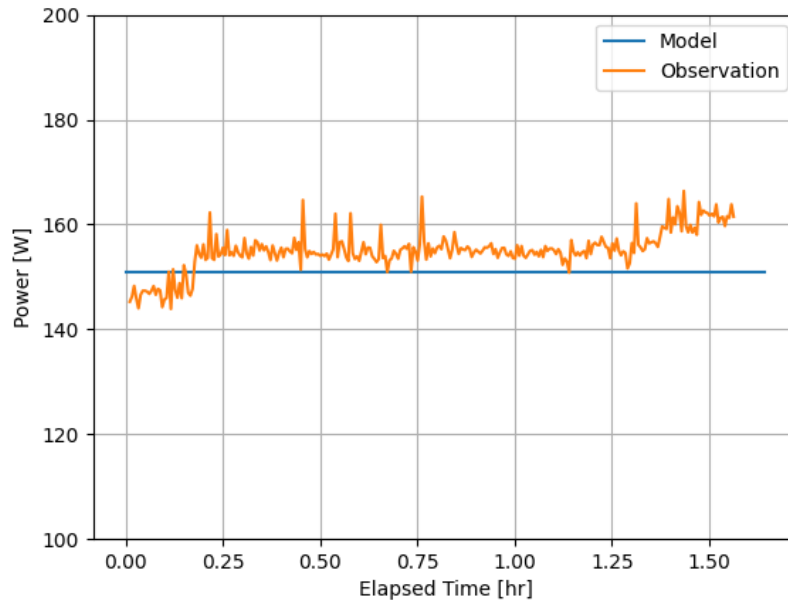
Figure 4.10. Time evolution of simulated vehicle power (blue) and observed vehicle power (red)

4.1.3   Mission Example: Transit Risk Reduction

Two example missions are presented to demonstrate how the combined power and environmental simulation environment form the basis of a TDA for UUV operations. Ensemble runs of the same mission at different start times provide insight into where mission risks may be present.

Mission Task: Conduct a no-fail single UUV mission to confirm or deny a sewage outfall near the Northern Wildlife Preserve in Mission Bay. Time window of operations is from 29-Jun-2022 to 01-Sep-2022. Predicted high sea state during the operational window requires pre-allocation of 66% of battery capacity to maintain loiter at the extraction point as a contingency to accommodate delays the recovery team might experience. All other aspects of the mission profile are left to the mission commander's discretion.

Examining hazards to navigation and high current areas, a start point (SP) was selected 2 km west of the Mission Bay entrance. After initialization and launch, the ingress route will travel 3 km at 080° through the main channel. Figure 4.11 illustrates that the planned route passes

under the West Mission Bay Drive and Ingraham Street bridges before entering the back bay to the objective area. The vehicle will continuously sample for presence/absence of sewage for the duration of the survey phase of the mission. The vehicle will commence egress immediately after arrival at the final ingress waypoint. Rather than exiting around Sail Bay, the vehicle will take the same route out of the bay to further reduce risk. Having developed the initial plan, the vehicle operator now has to consider the constraints listed in Table 4.1.
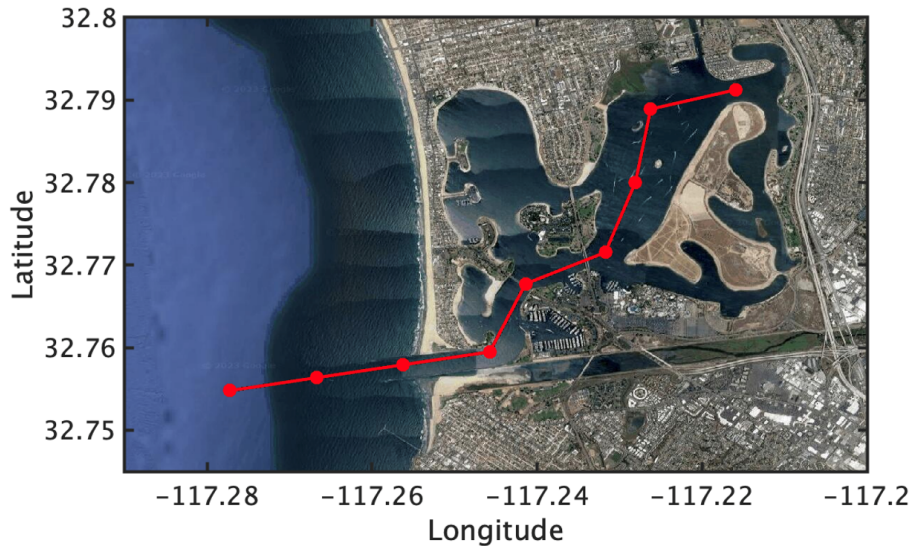
Figure 4.11. Waypoint route of harbor transit risk reduction mission. The 16 km long mission has 18 total waypoints with 1 km spacing.

Table 4.1. Harbor Transit Mission Constraints

Vehicle	REMUS 100
Operational window	29-Jun-2022 to 01-Sep-2022
Start/ end point	$32.76°$ N, $-117.26°$ E
Energy required at loiter location	66%

To examine the effect of vehicle propulsion mode setting, speed, and launch time on vehicle performance, an array of ensemble simulations of the planned mission was generated, covering a range of both constant ground speed and constant RPM mission modes. The constant speed configuration consisted of 10 ensemble simulations from 0.5 to 2.5 m/s at 0.25 m/s increments. The constant RPM experiment consisted of 14 ensemble simulations from 500 to

1800 RPM at 100 RPM increments. Each ensemble simulation began a mission every hour, on the hour, for the duration of the operational window (1537 hours).

Constant Speed Over Ground (SOG)

The pros and cons of the speed settings are presented in Table 3.1. Constant ground speed settings, for example, are desirable for seabed imaging with sidescan sonar. Sidescan is not a requirement of this mission, so the constant ground speed setting must merit selection based on energy consumption and risk alone.
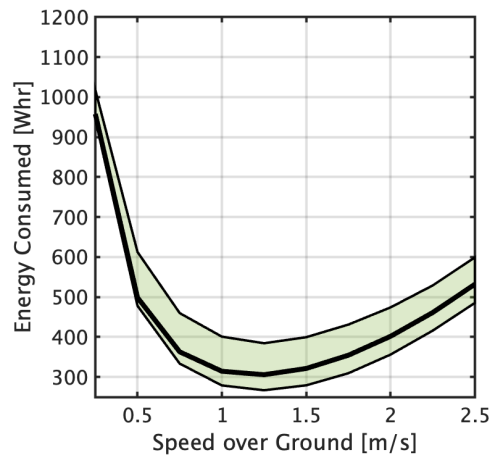
Figure 4.12. Minimum, maximum, and mean energy consumed for ten cSOG ensemble simulations from 0.25 m/s to 2.5 m/s at 0.25 m/s increments.

To better understand the energy consumption dynamics across all constant speed settings, Figure 4.12 shows the maximum, minimum, and mean energy consumption computed for the ensemble of simulations. The local minima at 1.25 m/s reveals the most power efficient setting for the vehicle. Note the asymmetry of the gains and losses where for this mission profile the energy penalties are approximately twice the size of the gains. For example, at 1.25 m/s the average mission consumes 300 Wh, the least efficient consumes 387 Wh, and the most efficient mission consumes only 266 Wh.
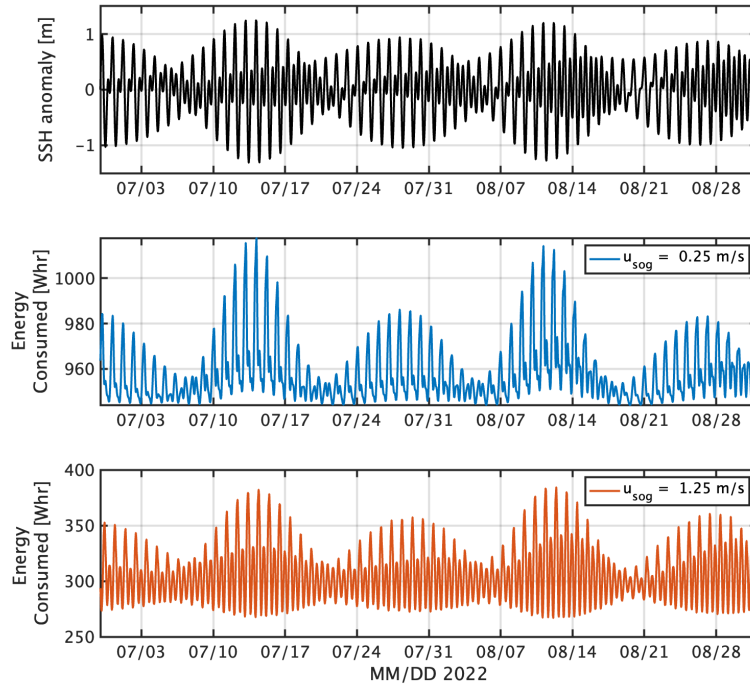
Figure 4.13. Time series of tidal amplitude at cSOG ensemble mission start times (black). Resulting energy consumption curves for the highest average of 0.25 m/s (blue) and lowest average 1.25 m/s (blue)

High values of energy consumption in Figure 4.13 correlate to spring tide swings, where periods of low deviation from the mean reveal the neap tide. Lower speed missions will take longer to complete, and thus be subject to the effects of currents for an extended time. The time to complete the mission relative is longer than a tidal period, and results in the scenarios of the vehicle fighting currents both ways, riding currents both ways, or alternating between head and tail currents for ingress and egress. As low speed missions will span one or more tidal cycles, the lowest magnitude current period will benefit the energy consumption disproportionately. Low speed cSOG mission are the only missions that have a power consumption minimum during a neap tide cycle.
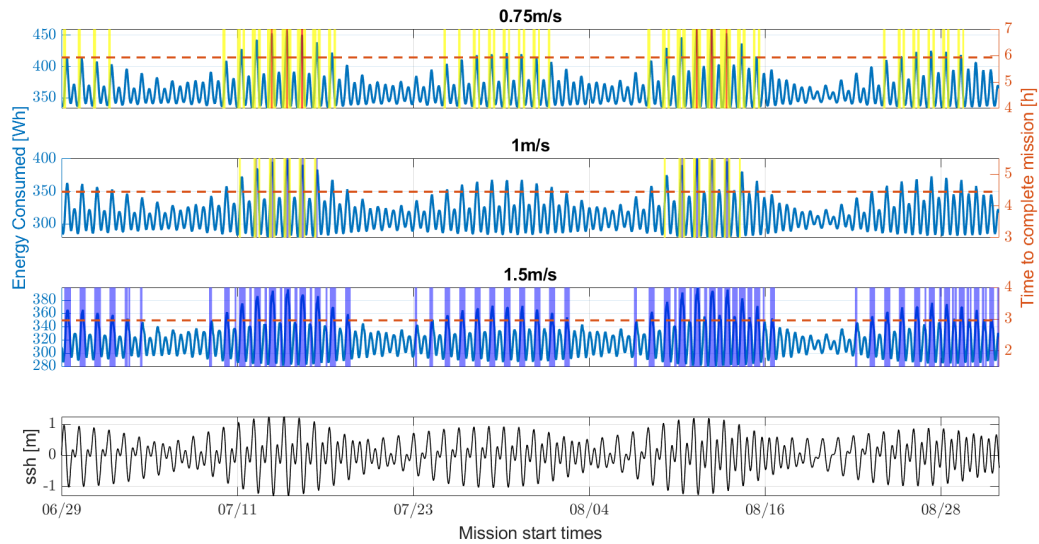
Figure 4.14. Time series of energy consumed (blue), mission length (red), sea surface height (black) with windows noting failure periods of steerage (yellow), head current (blue), and energy (red).
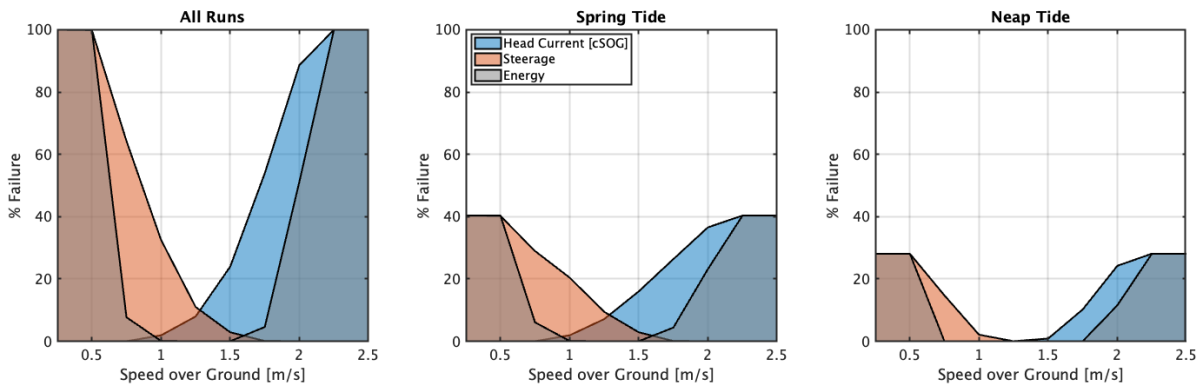
Figure 4.15. Head current (blue), steerage (red), and energy (gray) percent failure rate of missions based on programmed RPM and spring/neap tidal phase.

Figures 4.14 and 4.15 show a greater concentration of failures in spring tides and lower concentration of failures in neap tides. The local minima of failure rate occurs at 1.25 m/s for both tidal phases, indicating the lowest risk speed setting for this mission. Head current failures increase as the mission speed increases due to limited RPM buffer as defined by Table 3.3. In a no current environment, 2.25 m/s cSOG falls just below the RPM threshold, meaning that even

low head currents will require the vehicle to increase propeller RPM to maintain SOG, resulting in failure.

The greater the maximum current in an area, the lower the speed setting must be to provide the RPM ceiling necessary to avoid a head current failure. Conversely, steerage failures increase at slower speeds. High tail currents contribute to the SOG, yet the required speed through water and associated propeller speed decreases, reducing the efficacy of the fin control surfaces and ultimately steerage failures. Energy failures peak at the extremes of the speed scale, revealing that the longer duration of slow cSOG missions will consume more energy fighting head currents than they will gain riding any tail current. Faster cSOG missions, when faced with a head current, will increase thrust to the higher and less efficient RPM ranges to maintain the designated speed.

Constant RPM/Speed Through Water (cSTW)

The constant propeller speed RPM, or constant Speed Through Water (cSTW), control setting is the recommended propulsion mode setting for missions that transit through high current environments, as it eliminates steerage failures by maintaining a prescribed speed through water. The major failure related concern with a cSTW mission is that head currents may prevent the vehicle from making way along its intended track line. The two failure categories of leg timeout and head current quantify the failure risk in time and distance respectively. Vehicle SOG will vary depending on currents, thereby making time to complete mission variable. In this example mission, time to complete the mission is not a constraint.
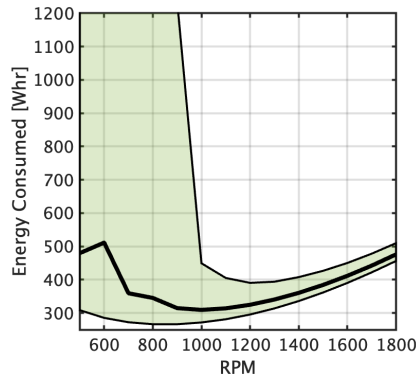
Figure 4.16. Minimum, maximum, and mean energy consumed for 14 cSTW ensemble simulations from 400 RPM to 1800 RPM at 100 RPM increments.

Figure 4.16 shows the maximum, minimum, and mean energy consumption recorded from the fourteen cSTW ensemble simulations. The most apparent trend occurs in the lower RPM range, where the energy losses well outweigh the energy gains until propeller speed reaches 1000 RPM. The most energy efficient mission occurs at 900 RPM, consuming 260 Wh; however the same speed setting also results in one of the least energy efficient simulated missions, consuming over 1200 Wh. After the vehicle setting exceeds 1000 RPM (1.3 m/s), the range of energy consumed drastically decreases. This line of demarcation in the speed scale is, interestingly, at the same speed as the maximum current in Mission Bay. This result demonstrates that if the vehicle can overcome the maximum current and still progress along the track line, it can finish the mission in reasonable time and time integrated impacts in regions of high current.
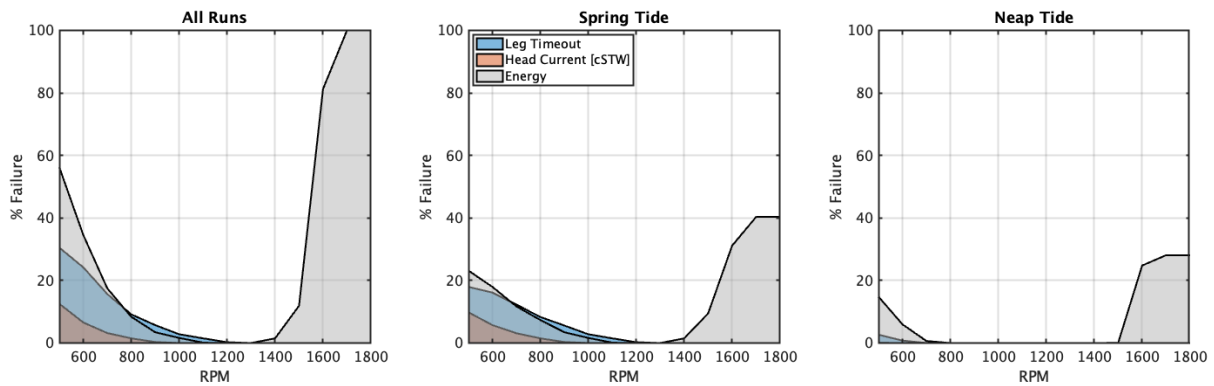
Figure 4.17. Leg timeout (blue), head current (red), and energy (gray) percent failure rate of missions based on programmed RPM and spring/neap tidal phase.

An analysis of cSTW failure criteria in Figure 4.17 reveals that the local minima falls at 1300 RPM with 0% failure. High magnitude currents in the spring tide period result in an even spread of failure types at the lower speed settings. The less power efficient speeds above 1300 RPM are much more susceptible to energy failures. Neap tide periods reveal a broader range of no failure mission speeds. Energy failures bracket the speed scale, with a few instances of leg timeout failure at the slowest speed.
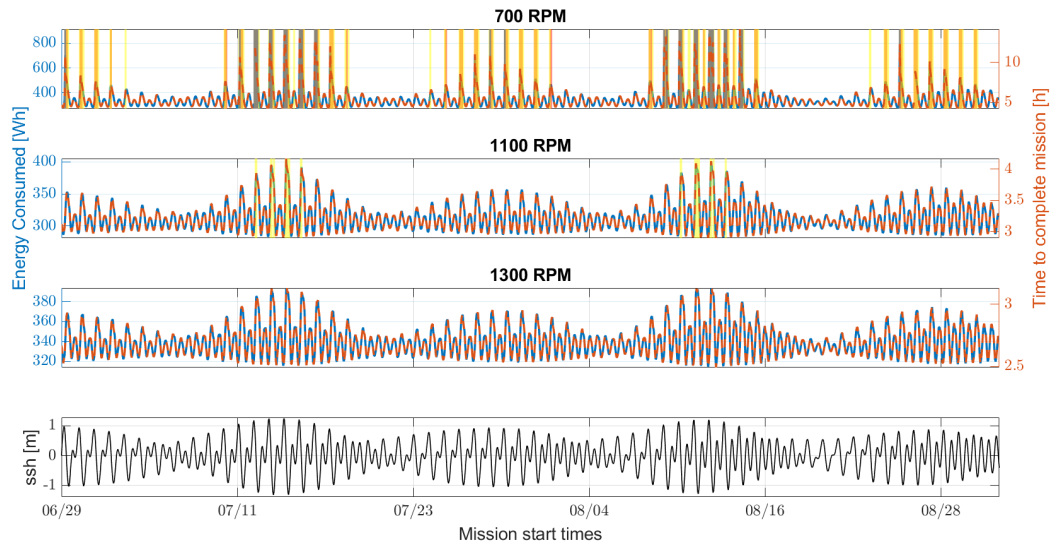
Figure 4.18. Time series of energy consumed (blue), mission length (red), sea surface height (black) with windows noting failure periods of leg failure (yellow), head current (blue), and energy (red).

In Figure 4.18, time series of the three primary failure criteria (energy, leg time out, head current) for each simulation are used to identify trends in the risk of the mission. An index associated with the proximity to failure, as defined in Chapter 3, is then created to provide a measure of failure risk. The criteria are presented as a percentage, with greater than 100% indicating a failure, and low values indicating low risk. Figure 4.19 presents the failure proximity for the mission run at 1100 RPM. To serve as a TDA, stoplight criteria are established for less than 50% (green), 51% to 85% (yellow), and greater than 85% (red). The two figures identify time windows of high risk (all failures signal in red zone), as well as windows that might have a

high probability of operational success. Presenting the time series of the index allows the mission planner to assess "all clear" time windows for safe operations. Similarly, due to the nature of time varying tides, there are time windows during spring tides that have low risk, quickly followed by time windows of high risk.
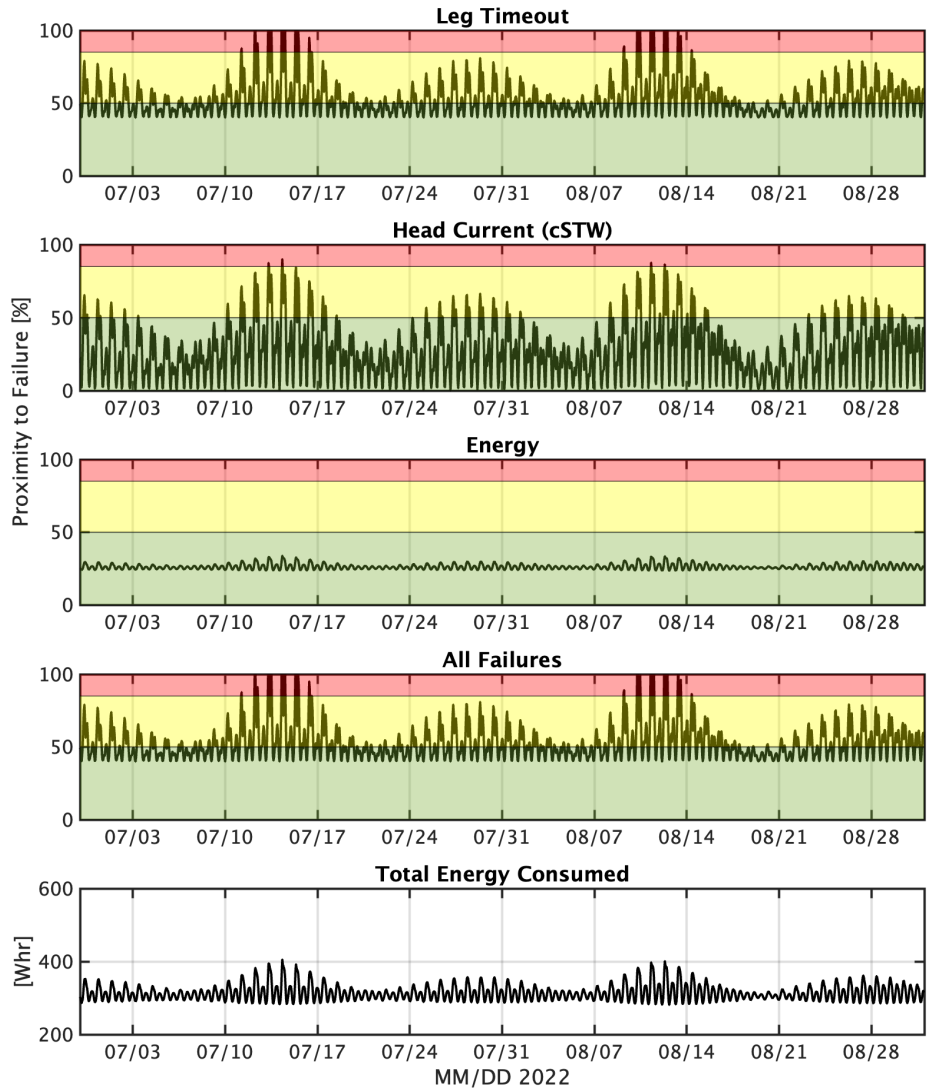
Figure 4.19. Proximity to failure for the described mission conducted with a fixed vehicle speed of 1100 RPM. In descending order, top to bottom: Leg Timeout, Head Current, Energy, and Union of all failures. Bottom: Total Energy Consumed for the mission.

Mission selection

Figures 4.20 and 4.21 provide the mission commander visual representations of time, space, and speed variation on performance metrics and failure criteria for the given mission to inform vehicle speed settings and launch time. A high rate of failure in spring tides and a very narrow window of no failure speeds in neap tides eliminate all cSOG settings for this mission. The 700 RPM to 1500 RPM range, resulting in 0% failure in neap tide periods, provides windows of time and speed ranges that result in low risk. Spring tides restrict the 0% failure window to 1300 RPM, but this speed opens the possibility of executing the mission at any point in the operational window. Programming the mission to run at 1300 RPM and executing during a neap tide may further reduce risk.
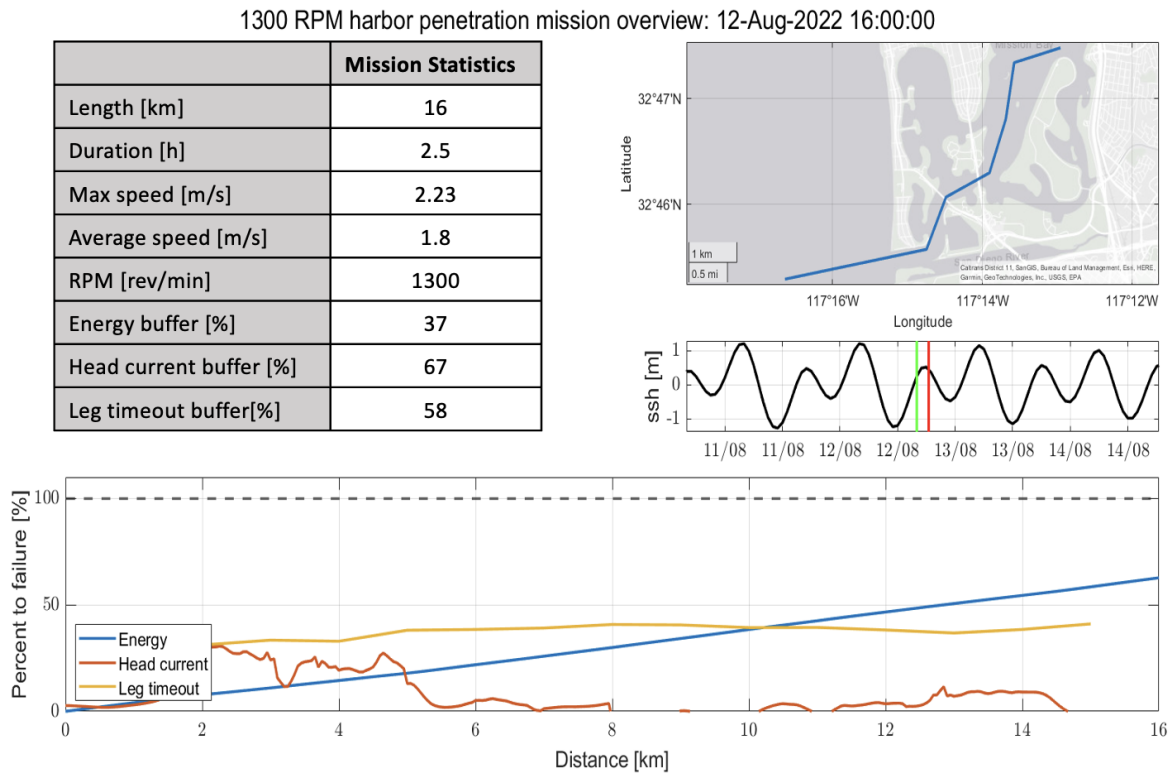
Figure 4.20. Data sheet and mission overview of the statistically lowest risk mission.

After down selecting cSOG and identifying 1300 RPM as the optimal cSTW setting, each of the 1537 ensembles were examined for this speed setting. Non-dimensionalization of the

failure criteria allows the mission commander to assess a safety factor or buffer of failure. The failure category with the lowest buffer percentage will be used to define the overall margin of risk to the mission.

Figure 4.20 shows the 1300 RPM cSTW risk reduction harbor penetration mission executed on 12-Aug-2022 at 16:00:00 with the greatest absolute buffer. Launched at a slack tide within a spring tide cycle, this mission runs in 2.5 hours with an average SOG of 1.8 m/s. A 37% energy, 67% head current, and 59% leg timeout resulting in a 37% overall risk margin for the mission.
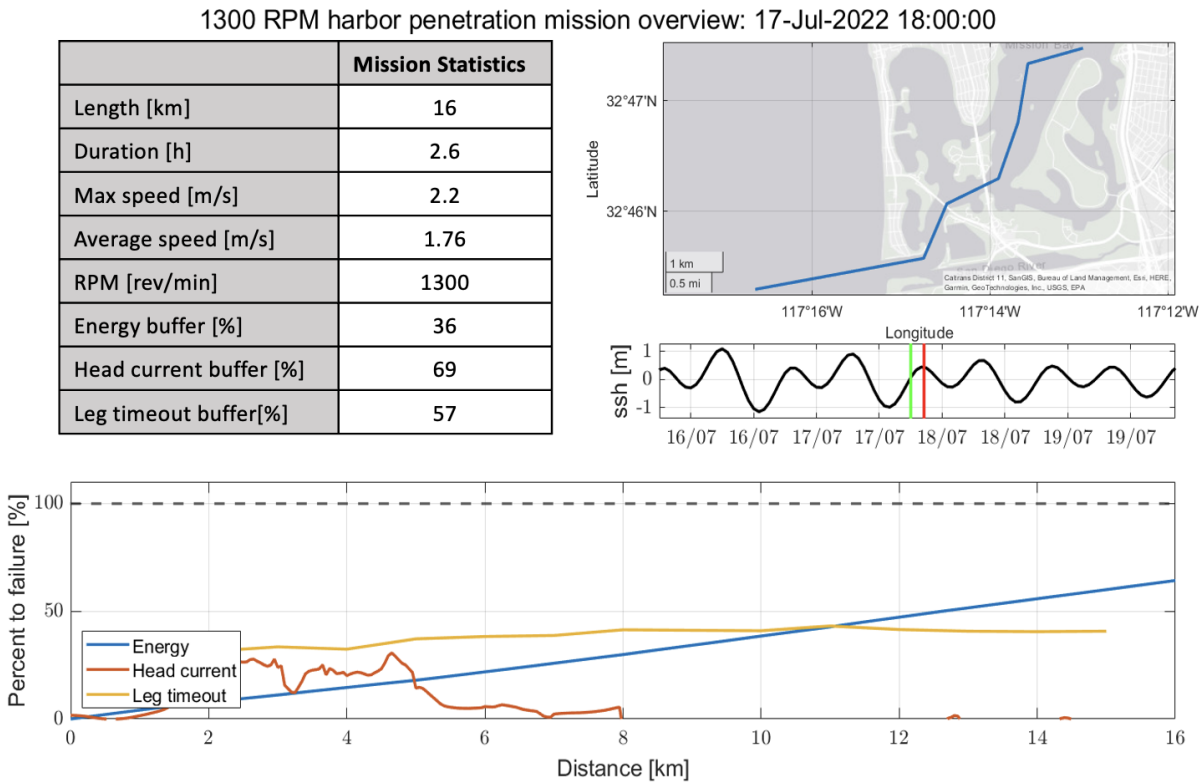
Figure 4.21. Mission commander's selection. The mission data sheet identifies the time and settings for a low relative risk (and uncertainty of risk) from launch at the beginning of the spring tidal phase.

Considering human error, timeline delays, and the high variation of performance metrics in spring tide periods, the mission commander selected a mission start time within a neap tide cycle. The mission with the greatest overall buffer margin has a launch time of 18:00:00 on

17-Jul-2022. Figure 4.21 shows the launch and recovery straddling a slack tide at the beginning of a neap tide cycle. The mission loses 2% overall buffer, but gains 2% buffer for both head current and leg timeout failures. The vehicle operator now has much greater flexibility in mission launch time should the schedule be compromised.

4.1.4   Mission Example: Survey Optimization

Mission Task: The previous transit risk reduction mission successfully detected the presence of contaminated water from a sewage outfall near the Northern Wildlife Preserve in Mission Bay. Conduct a single side scan sonar mission of Sail Bay in Mission Bay to identify the outfall discharge, see Figure 4.22. The commander is authorized to accept moderate risk to mission and risk to vehicle to maximize survey area. The altered mission objectives result in the constraints listed in Table 4.2.
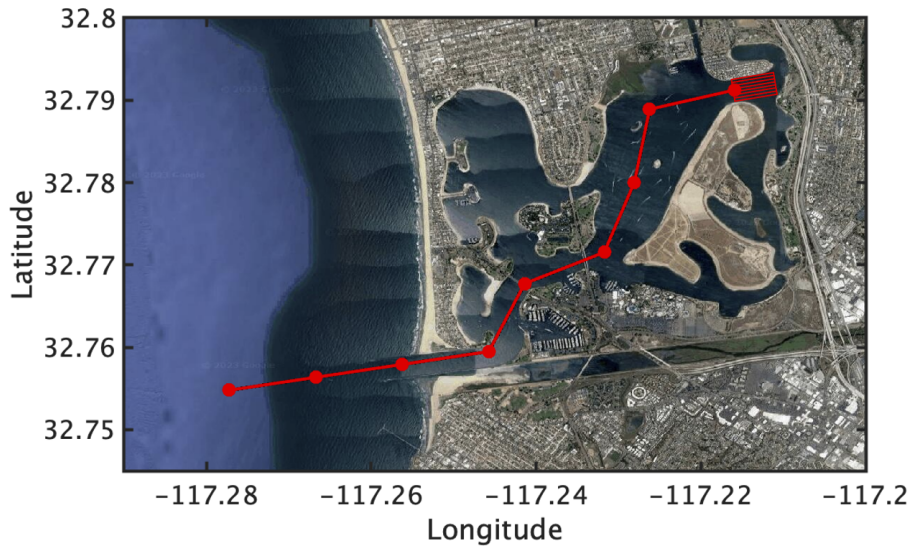
Figure 4.22. Waypoint route of harbor transit and survey area (red box).

Table 4.2. Survey Optimization Mission Constraints

Vehicle	REMUS 100
Operational window	18-Jul-2022 to 01-Sep-2022
Centroid of survey area	32.76° N, $-117.26°$ E
Survey speed	1 m/s or 1.5 m/s
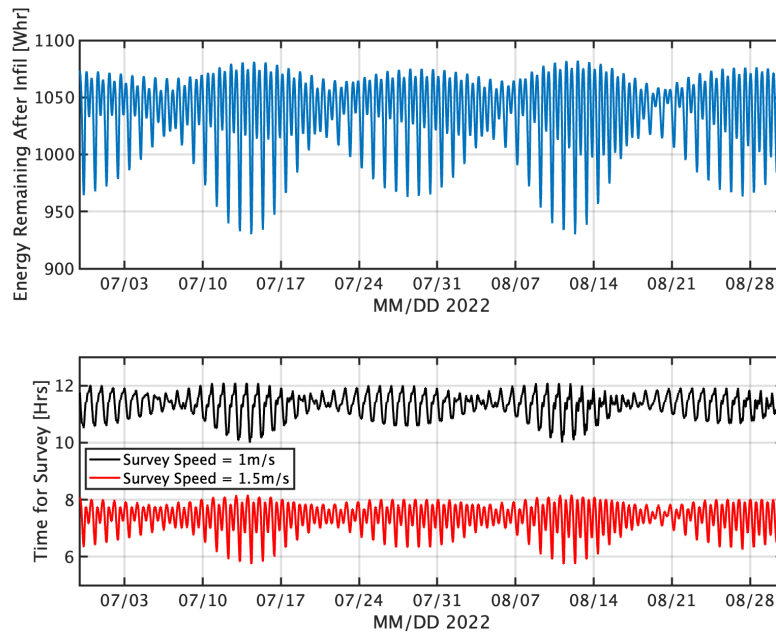
Figure 4.23. (Top) Time series of energy remaining for survey and exfiltration showing spring/neap tidal variability. (Bottom) Survey hours available as a function of time and survey speed.

The transit risk reduction analysis identified 1.5 m/s constant SOG as the desired transit speed to reduce risk of failure and maintain good energy efficiency. To optimize loiter time, the mission is separated into egress and ingress ensemble simulations. The ingress ensemble provides the energy consumed (variable) and the mission run time (constant). By subtracting energy consumed during ingress from the total battery capacity of 1200 Watt hours, we can identify the power remaining for survey and egress. From the energy remaining after ingress value, iterative calculations using 1 m/s and 1.5 m/s cSOG with no currents were stepped through time at 5 minute intervals.

Each interval queried the reduced ordered model of energy required for vehicle egress. Once the sum of these values exceed the energy remaining after ingress, the change in time is recorded as maximum survey time. Figure 4.23 shows the same spring/neap pattern with losses relative to the mean having a larger amplitude than gains in survey time.
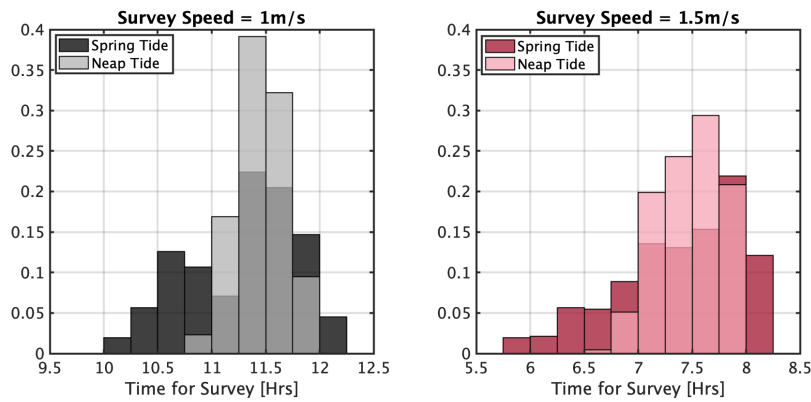
Figure 4.24. Distribution of hours available for survey based on survey speed and spring/neap tidal phase.

The distribution of survey time, displayed in Figure 4.24, is skewed towards higher values. This result implies that there is an opportunity to find conditions that lead to extended survey times. Note that survey times are also higher when the survey speed is slower. The total survey lengths are calculated and shown in Table 4.3 for the two assumed survey speeds. The mean distance of both survey speeds is similar; however, the 1.5 m/s survey speed yields the longest survey distance travelled.

Table 4.3. Optimized Survey Length

Survey Speed	1 m/s	1.5 m/s
Average	41 km	41 km
Maximum	39.6 km	43.74 km
Minimum	36 km	31.3 km

Mission selection

Figure 4.24 and Table 4.3 documents the high risk of surveying at 1.5 m/s but the potential to maximize the survey area with appropriate timing and speed settings that exploits the environment. The survey stands to gain 10% longer survey distance by operating at 1.5 m/s versus 1 m/s. Additionally, the survey will be four hours shorter than a 1 m/s survey. To maximize survey area, the vehicle operator should execute the survey mission on the 07/14

incoming tide at a survey speed of 1.5 m/s.

4.2   TDA Lessons Learned

The TDA displays illustrated in this thesis help the mission commander to make informed decisions regarding mission start time, propulsion mode setting, vehicle speed, and vehicle route. This control allows for risk mitigation of four separate failure criteria by providing quantitative buffer margin percentages.

The TDA visualizations provide valuable insight into vehicle performance, which was only previously available from post-mission analysis. This information is useful in refining the mission parameters in the planning phase, and can be extremely helpful in planning for contingency operations. In the event of a lost vehicle, the latitude and longitude correlated to areas with the highest risk of failure can serve as an initial starting location for search operations for a lost vehicle in the absence of additional information.

Although the DELFT 3D model and simulation environment have been validated, the accuracy is not quantified for all possible applications. The mission commander will have to make a judgement on how much trust to place in the model and simulation output when considering the information presented in the TDA. This trust can be built through work-ups that validate the performance of the simulation environment.

Chapter 5

Conclusion

The primary objective of the planning process is to assess feasibility of meeting mission requirements and reducing risk. Incorporation of environmental information into the UUV mission planning process reduces risk by the identification of the various current-driven failure modes: total available energy, time outs, and adverse vehicle flight performance.

The energy required to complete a mission is influenced by water current regardless of the chosen navigation mode (constant propeller or ground speed). Besides avoiding mission failure, adapting to water currents holds promise for optimizing the vehicle route and mission time window; eg. designing missions that consume the least amount of battery energy.

Strong water currents may also affect vehicle safety. A significant current opposing vehicle motion may impede forward progress. A water current following the vehicle (tail current) can affect vehicle stability and control. Predicting conditions that may lead to mission failure is a desired outcome of mission planning. Similarly, currents may impact the time required to execute a mission. Accurate predictions of mission time are critical for naval operations that depend on prior knowledge of mission start and end times.

This thesis developed and implemented a simulation framework for the purpose of incorporating environmental information in UUV mission plans. The simulation framework is built from a simplified vehicle power model that assumes the vehicle operates at a constant depth in either a constant propeller speed or constant ground speed modes.

Water current information is incorporated in the simulation as tabular data defined on a uniform grid of location and time. To achieve the most useful results, the current environment should match the time scales and spatial resolution of the intended mission. The fidelity of a simulation framework, incorporating a power model for a small-diameter UUV and the DELFT3D ocean current model, was verified by comparing simulation predictions to fixed sensor measurements and vehicle flight tests.

The completed simulation framework forms the basis for a UUV operations TDA. The TDA allows the user to perform a rapid analysis of alternatives. It has two primary benefits. Firstly, the user can balance mission objectives, including reduced energy use, against the risk of mission failure. Two sample mission scenarios demonstrate how the best operating conditions can be found among many trials. Secondly, the ability to generate statistics from an ensemble of alternatives can reveal trends that guide the overall planning process and build operator intuition. For example, it may be discovered that vehicle deployment during specific tidal phases offers both a high level of safety and reduced energy use.

This thesis has resulted in a prototype TDA. To continue its development, the TDA should be exercised on a much larger variety of vehicles and environments. In particular, the TDA should be tested with larger vehicles intended for long endurance missions. Continued study of environmental models should also be undertaken, with the intent to characterize uncertainty in these models and the effect this uncertainty has on the resulting mission plans.

Understanding the effects of currents on vehicle performance is difficult for UUV operators to assess without use of computational tools, accurate knowledge of the environment, and validated vehicle power consumption models. This thesis uses a systematic approach to predicting and displaying vehicle performance in realistic ocean current environments and shows it to be a powerful tool in improving mission planning processes, optimizing vehicle performance, and reducing risk to the mission or vehicle. Rapid assessment of a highly complex mission holds value to real-world Naval missions in which the mission must be adapted to in near-real-time by the commander. This advanced preparation can save critical pre-mission analysis time that might

be better allocated to vehicle pre-mission checks or coordination with supporting assets.

Future work identified with this thesis includes quantifying model and simulation uncertainty, and carrying it forward through the simulation to provide a more accurate depiction of the sensitivity to risk and performance metrics. This thesis also aims to inform the implementation of onboard alogrithms. Transition to onboard decision-making based on real-time sensing remains a goal for environmentally adaptive autonomy.

Bibliography

[1] "Operational Risk Management (ORM) - Safety - Naval Postgraduate School."

[2] C. von Alt, B. Allen, T. Austin, N. Forrester, R. Goldsborough, M. Purcell, and R. Stokey, "Hunting for mines with REMUS: a high performance, affordable, free swimming underwater robot," in *MTS/IEEE Oceans 2001. An Ocean Odyssey. Conference Proceedings (IEEE Cat. No.01CH37295)*, vol. 1, pp. 117–122 vol.1, Nov. 2001.

[3] R. Bachmayer, B. Deyoung, C. Williams, C. Bishop, C. Knapp, and J. Foley, "Development and deployment of ocean gliders on the Newfoundland Shelf," Jan. 2006.

[4] R. N. Smith, J. Kelly, and G. S. Sukhatme, "Towards improving mission execution for autonomous gliders with an ocean model and kalman filter," in *2012 IEEE International Conference on Robotics and Automation*, pp. 4870–4877, May 2012. ISSN: 1050-4729.

[5] N. Von Oppeln-Bronikowski, M. Zhou, and B. deYoung, "Improving path-planning for glider operations: A current-forecast based approach applied in the Gulf of St. Lawrence," preprint, Oceanography, Nov. 2021.

[6] T. Gerkema, *An Introduction to Tides*. Cambridge: Cambridge University Press, 2019.

[7] A. D'Alpaos, S. Lanzoni, M. Marani, and A. Rinaldo, "On the tidal prism–channel area relations," *Journal of Geophysical Research: Earth Surface*, vol. 115, no. F1, 2010. _eprint: https://onlinelibrary.wiley.com/doi/pdf/10.1029/2008JF001243.

[8] K. Carroll, S. McClaran, E. Nelson, D. Barnett, D. Friesen, and G. William, "AUV path planning: an A* approach to path planning with consideration of variable vehicle speeds and multiple, overlapping, time-dependent exclusion zones," in *Proceedings of the 1992 Symposium on Autonomous Underwater Vehicle Technology*, pp. 79–84, June 1992.

[9] Y. Singh, S. Sharma, R. Sutton, D. Hatton, and A. Khan, "A constrained A* approach towards optimal path planning for an unmanned surface vehicle in a maritime environment containing dynamic obstacles and ocean currents," *Ocean Engineering*, vol. 169, pp. 187–201, Dec. 2018.

[10] A. Alvarez, A. Caiti, and R. Onken, "Evolutionary path planning for autonomous underwater vehicles in a variable ocean," *IEEE Journal of Oceanic Engineering*, vol. 29, pp. 418–429, Apr. 2004. Conference Name: IEEE Journal of Oceanic Engineering.

[11] H. Durrant-Whyte and T. Bailey, "Simultaneous localization and mapping: part I," *IEEE Robotics & Automation Magazine*, vol. 13, pp. 99–110, June 2006. Conference Name: IEEE Robotics & Automation Magazine.

[12] J. David Hernández, E. Vidal, G. Vallicrosa, Pairet, and M. Carreras, "Simultaneous mapping and planning for autonomous underwater vehicles in unknown environments," in *OCEANS 2015 - Genova*, pp. 1–6, May 2015.

[13] M. Soulignac, "Feasible and Optimal Path Planning in Strong Current Fields," *IEEE Transactions on Robotics*, vol. 27, pp. 89–98, Feb. 2011. Conference Name: IEEE Transactions on Robotics.

[14] B. Garau, A. Alvarez, and G. Oliver, "Path Planning of Autonomous Underwater Vehicles in Current Fields with Complex Spatial Variability: an A* Approach," in *Proceedings of the 2005 IEEE International Conference on Robotics and Automation*, pp. 194–198, Apr. 2005. ISSN: 1050-4729.

[15] W. Hong-jian, B. Xin-qian, Z. Xu, F. Ming-yu, and L. Juan, "Two approaches for autonomous underwater vehicle global path planning in large range ocean environment," in *2004 International Conference on Intelligent Mechatronics and Automation, 2004. Proceedings.*, pp. 224–227, Aug. 2004.

[16] Z. Hong-han, G. Liming, C. Tao, W. Lu, and Z. Xun, "Global path planning methods of UUV in coastal environment," in *2016 IEEE International Conference on Mechatronics and Automation*, pp. 1018–1023, Aug. 2016. ISSN: 2152-744X.

[17] A. J. Healey and D. B. Marco, "Slow Speed Flight Control of Autonomous Underwater Vehicles: Experimental Results with NPS AUV II,"

[18] B. Fletcher, "UUV master plan: a vision for navy UUV development," in *OCEANS 2000 MTS/IEEE Conference and Exhibition. Conference Proceedings (Cat. No.00CH37158)*, vol. 1, (Providence, RI, USA), pp. 65–71, IEEE, 2000.

[19] R. Panish and M. Taylor, "Achieving high navigation accuracy using inertial navigation systems in autonomous underwater vehicles," in *OCEANS 2011 IEEE - Spain*, pp. 1–7, June 2011.

[20] D. Kruger, R. Stolkin, A. Blum, and J. Briganti, "Optimal AUV path planning for extended missions in complex, fast-flowing estuarine environments," in *Proceedings 2007 IEEE International Conference on Robotics and Automation*, pp. 4265–4270, Apr. 2007. ISSN: 1050-4729.

[21] X. Chen, N. Bose, M. Brito, F. Khan, B. Thanyamanta, and T. Zou, "A Review of Risk Analysis Research for the Operations of Autonomous Underwater Vehicles," *Reliability Engineering & System Safety*, vol. 216, p. 108011, Dec. 2021.

[22] M. P. Brito, G. Griffiths, and P. Challenor, "Risk Analysis for Autonomous Underwater Vehicle Operations in Extreme Environments," *Risk Analysis*, vol. 30, no. 12, pp. 1771–1788, 2010. _eprint: https://onlinelibrary.wiley.com/doi/pdf/10.1111/j.1539-6924.2010.01476.x.

[23] C. A. Thieme and I. B. Utne, "A risk model for autonomous marine systems and operation focusing on human–autonomy collaboration," *Proceedings of the Institution of Mechanical Engineers, Part O: Journal of Risk and Reliability*, vol. 231, no. 4, pp. 446–464, 2017. Publisher: SAGE Publications Sage UK: London, England.

[24] J. E. Bremnes, P. Norgren, A. J. Sørensen, C. A. Thieme, and I. B. Utne, "Intelligent Risk-Based Under-Ice Altitude Control for Autonomous Underwater Vehicles," in *OCEANS 2019 MTS/IEEE SEATTLE*, pp. 1–8, Oct. 2019. ISSN: 0197-7385.

[25] B. K. Evans, *The effect of coded signals on the precision of autonomous underwater vehicle acoustic navigation*. Thesis, Massachusetts Institute of Technology, 1999. Accepted: 2005-09-27T20:16:14Z ISSN: 4339-7344.

[26] J. Chang, M. Anderson, S. Merrifield, A. Nager, R. Hess, R. Young, S. Kitchen, and E. Terrill, "Power Efficiency Autonomy for Long Duration AUV Operation," in *2022 IEEE/OES Autonomous Underwater Vehicles Symposium (AUV)*, pp. 1–6, Sept. 2022. ISSN: 2377-6536.

[27] "Delft3D-FLOW User Manual."

[28] E. Glaessgen and D. Stargel, "The digital twin paradigm for future NASA and U.S. air force vehicles," Apr. 2012.

[29] Y. Song, Y. Wang, S. Yang, S. Wang, and M. Yang, "Sensitivity analysis and parameter optimization of energy consumption for underwater gliders," *Energy*, vol. 191, p. 116506, Jan. 2020.

[30] R. Young, S. Merrifield, M. Anderson, and E. Terrill, "A Simulation Framework for Environmentally-Aware Autonomous Underwater Vehicle (AUV) Mission Planning and Algorithm Development," *OCEANS 2023: Gulf Coast*, 2023.

[31] W. J. Herron, "Case History of Mission Bay Inlet, San Diego, California," pp. 801–821, Dec. 2015. Publisher: American Society of Civil Engineers.

[32] K. Schiff and P. Kinney, "Tracking Sources of Bacterial Contamination in Stormwater Discharges to Mission Bay, California," *Water Environment Research*, vol. 73, no. 5, pp. 534–542, 2001. _eprint: https://onlinelibrary.wiley.com/doi/pdf/10.2175/106143001X139605.